

Generation and performance assessment of the global TanDEM-X digital elevation model

Paola Rizzoli*, Michele Martone, Carolina Gonzalez, Christopher Wecklich, Daniela Borla Tridon, Benjamin Bräutigam, Markus Bachmann, Daniel Schulze, Thomas Fritz, Martin Huber, Birgit Wessel, Gerhard Krieger, Manfred Zink, Alberto Moreira

German Aerospace Center (DLR), Oberpfaffenhofen, Germany



ARTICLE INFO

Article history:

Received 2 February 2017

Received in revised form 17 August 2017

Accepted 22 August 2017

Keywords:

TanDEM-X
Bistatic SAR
Digital elevation model (DEM)
Interferometry
Remote sensing

ABSTRACT

The primary objective of the TanDEM-X mission is the generation of a global, consistent, and high-resolution digital elevation model (DEM) with unprecedented global accuracy. The goal is achieved by exploiting the interferometric capabilities of the two twin SAR satellites TerraSAR-X and TanDEM-X, which fly in a close orbit formation, acting as an X-band single-pass interferometer. Between December 2010 and early 2015 all land surfaces have been acquired at least twice, difficult terrain up to seven or eight times. The acquisition strategy, data processing, and DEM calibration and mosaicking have been systematically monitored and optimized throughout the entire mission duration, in order to fulfill the specification. The processing of all data has finally been completed in September 2016 and this paper reports on the final performance of the TanDEM-X global DEM and presents the acquisition and processing strategy which allowed to obtain the final DEM quality. The results confirm the outstanding global accuracy of the delivered product, which can be now utilized for both scientific and commercial applications.

© 2017 The Authors. Published by Elsevier B.V. on behalf of International Society for Photogrammetry and Remote Sensing, Inc. (ISPRS). This is an open access article under the CC BY license (<http://creativecommons.org/licenses/by/4.0/>).

1. Introduction

Digital elevation models are of fundamental importance for a large variety of scientific and commercial applications. For example, precise and up-to-date information about the Earth's topography is required in many geoscience areas, such as geology, forestry, glaciology, oceanography, and hydrology. Up to now, the primary source of elevation data on an almost global scale has been provided by the Shuttle Radar Topography Mission (SRTM), characterized by a spatial resolution of 30 m between 56° South latitude and 60° North latitude (Farr et al., 2007). Moreover, the ASTER and the AW3D30 DEMs are available with a 30 m posting: the first one covers latitudes between 83° South and 83° North (Meyer et al., 2011), while the second one presents numerous gaps in both Antarctica and arctic regions (Tadono et al., 2016). For higher latitudes and over Antarctica, only lower resolution (on the order of hundred meters to kilometers) DEMs are available, such as GTOPO (GTOPO, 2016), GLOBE (Hastings et al., 1999), RAMP (RAMP, 2016), and GLAS/ICESat (ICESat, 2016).

With the main goal of acquiring a global and consistent DEM with unprecedented accuracy, the TanDEM-X mission (TerraSAR-X add-on for Digital Elevation Measurements) opens a new era in spaceborne synthetic aperture radar (SAR) (Krieger et al., 2007, 2013). Developed in a public-private partnership between the German Aerospace Center (DLR) and Airbus Defence and Space, it is comprised of two almost identical satellites, TerraSAR-X and TanDEM-X, equipped with a synthetic aperture radar operating at X-band. Since October 2010, both satellites have been flying in a close orbit configuration at an altitude of around 500 km, as presented in Fig. 1, acting as a single-pass SAR interferometer and allowing for a flexible selection of baselines and acquisition geometries. Images have been nominally acquired in bistatic configuration, where one satellite transmits and both simultaneously receive the backscattered signal from the Earth's surface. This enables the acquisition of highly accurate interferograms, which do not suffer from temporal and atmospheric decorrelation.

A dedicated acquisition strategy has been developed and optimized throughout the years, in order to achieve the desired performance on a global scale. Both satellites have been flying in the so-called Helix orbit, which combines an out-of-plane orbital displacement with a radial (vertical) separation resulting in a

* Corresponding author.

E-mail address: Paola.Rizzoli@dlr.de (P. Rizzoli).

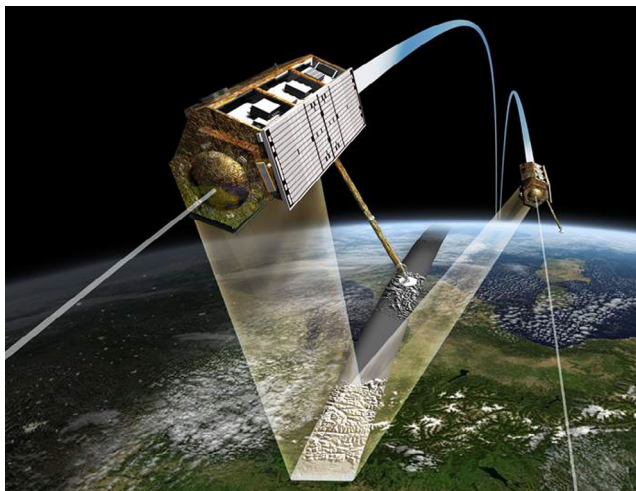


Fig. 1. Artist's view of TerraSAR-X and TanDEM-X satellites flying in close orbit formation.

helix-like relative movement of the satellites along the orbit, avoiding the collision risk at the poles (Moreira et al., 2003; Moreira et al., 2004). Driven by the DEM accuracy specifications the Helix formation has been continuously optimized during different mission acquisition phases.

Beyond the generation of a global DEM, the unique configuration of TanDEM-X also allows for the demonstration of innovative bistatic SAR techniques, such as multistatic SAR, polarimetry, interferometry, digital beam forming and superresolution. Hence, TanDEM-X also represents a milestone for the development of future spaceborne formation-flying SAR missions, such as Tandem-L, an L-band bistatic SAR mission proposed by DLR, with the goal of monitoring dynamic processes on the Earth surface with unprecedented accuracy and temporal coverage (Moreira et al., 2015).

The objective of this paper is to assess the final performance of the TanDEM-X global DEM. After an overview of the TanDEM-X mission and its specification, the error sources affecting the quality of the DEM are summarized, together with the developed acquisition strategy and processing chain. Finally, the global performance is then assessed in terms of vertical accuracy and coverage statistics. All specified performance parameters for the DEM accuracy have been achieved or even surpassed.

2. TanDEM-X mission overview

In this section, the TanDEM-X DEM specifications are reported, together with the interferometric processing chain for a single scene DEM. The error sources affecting the final performance are discussed as well, together with the implemented strategy for overcoming such limitations, in terms of acquisition planning optimization, calibration procedures, and DEM mosaicking. The pre-

sentation of the required steps for generating the final DEM is focusing on the most relevant approaches to ensure the final TanDEM-X DEM quality.

2.1. Mission performance specification

The global DEM delivered by TanDEM-X has been defined to meet or exceed the specification presented in Table 1, as in the TanDEM-X DEM product specification document (Wessel, 2016). The main parameters which are taken into account for assessing the final performance are summarized and explained in the following:

- The *DEM spatial resolution* (or independent spacing): For the global DEM interferometric data have been acquired in Strip-Map mode with a resolution of 3.3 m (Fritz and Eineder, 2013). Spatial multilooking is then applied in order to reduce the noise affecting the interferometric phase, which allows to generate a DEM with an independent ground pixel spacing of 12 m × 12 m at the Equator, referred to the WGS84 ellipsoid.
- The *absolute vertical height accuracy* is defined as the uncertainty in the height of a point with respect to the WGS84 ellipsoid caused by random and uncorrected systematic errors. The specified value is expressed as a linear error at a 90% confidence interval. The digital elevation information is defined with respect to the reflective surface of X-band interferometric SAR returns from the imaged Earth features, estimating therefore the location of the mean phase center resulting from a single or multiple backscattered signals within the same resolution cell. The data may hence include height offsets due to penetration into vegetation canopies or ice/snow-covered regions and possible seasonal variations. The specified absolute vertical accuracy of the global DEM shall be better than 10 m.
- The *relative vertical height accuracy* is defined as the uncertainty between two height estimates caused by random errors. The specified values are expressed as linear errors at a 90% confidence interval. The relative vertical accuracy shall be smaller than 2 m for low and medium relief terrain (predominant slope lower than 20%) and 4 m for high relief terrain (predominant slope greater than 20%), over a 1° × 1° geocell in latitude/longitude.
- The *absolute horizontal accuracy* is defined as the uncertainty in the horizontal position of a point with respect to WGS84 caused by random and uncorrected systematic errors. The value is expressed as a circular error at the 90% confidence level. The absolute horizontal accuracy shall be better than 10 m.
- The *voids or Invalid Data*: areas in the DEM that are left void (i.e. no data) may occur for several reasons, including poor signal-to-noise ratio (SNR) over sandy desert areas, shadow and layover in mountains and canyons, DEM gaps which result from the absence of acquired data or input DEMs with satisfying quality, or decorrelated water areas such as lakes and oceans. According to the mission specification, at most 3% of all DEM pixels over land-covered areas (water bodies excluded) can be flagged as

Table 1
TanDEM-X DEM specification parameters.

Requirement	Description	Specification
Relative vertical accuracy	90% linear point-to-point error over a 1° × 1° cell	2 m (slope <20%) 4 m (slope >20%)
Absolute vertical accuracy	90% linear error	10 m
Absolute horizontal accuracy	90% circular error	10 m
Spatial resolution	Independent pixels	12 m (0.4 arc sec @ equator)
Coverage	Percentage of land masses	97%

invalid. As for the absolute vertical accuracy, but unlike the relative vertical accuracy, the percentage of voids is evaluated on a global scale and not on a geocell basis.

2.2. Precise baseline calibration

The precise knowledge of the baseline between the two satellites is of fundamentally important for deriving highly accurate DEMs. The required accuracy in baseline determination is in the order of 1 mm, which corresponds to a vertical offset on the order of 1 m. Coarse baseline determination is performed by a double differential evaluation of GPS carrier phase measurements (Zhu et al., 2004; Wermuth et al., 2011). However, the relative satellite positions derived from GPS measurements are biased, mainly due to uncompensated offsets from the SAR antenna phase centers, which results in offsets up to 10 mm (Hueso Gonzalez et al., 2012). For precise calibrating baselines, globally distributed flat test sites with known topographic height are repeatedly acquired. In this way, initial offsets can be estimated and corrected, allowing for a monitoring of the baseline stability over time. The long-term evolution of the baseline bias radial and along-track components from 2010 up to 2014 is shown in Fig. 2: the measurements show a standard deviation of 1.31 mm (Hueso Gonzalez et al., 2012; Walter Antony et al., 2013). The estimated offsets are finally applied to obtain the calibrated baseline, which is used for Raw DEM processing, as presented in Section 2.3.

2.3. Processing single-pass interferometric data

The Integrated TanDEM-X Processor (ITP) (Fritz et al., 2011) processes the interferometric bistatic raw data from the TerraSAR-X and TanDEM-X instruments to pre-calibrated and geocoded single-scene DEMs, so-called RawDEMs, the building blocks of the mosaicked final DEM. The ITP thus comprises data take screening, focusing and interferometric processing steps. By delivering direct feedbacks on acquisition quality via several quality check products, the ITP was involved in the acquisition process and triggered immediate reacquisition of erroneous data and/or changes in the acquisition plans (see Section 2.5) to ensure a complete coverage and avoid the inclusion of distorted DEM data in the final product. To generate unbiased, independent, and absolute height information, the ITP does not use any external reference data in its height calibration chain but relies on the precise calibration of the system, which comprises the compensation of the SAR antenna phase patterns and the correction of the SAR instrument phase drifts by applying the internal calibration replica and correction procedure (Bräutigam et al., 2010). This poses some challenges on the processing chain with respect to the specific characteristics of single-pass interferometric data from two instruments. Only those steps which are of higher relevance regarding the TanDEM-X DEM performance are highlighted in the following paragraphs. The most critical step in terms of larger DEM errors, the phase unwrapping, is detailed in Section 2.4.

- **Synchronization:** The two on-board oscillators are independent and have to be synchronized to ensure that the interferometric phase differences correspond only to the topographic signal. Therefore, synchronization pulses are exchanged between the satellites and analyzed by the ITP for phase correction of the passive instrument to the master frequency. Besides overall frequency offsets some significant short time variations in the relative phase drifts are also present and need to be corrected in order to avoid height errors waves of several meters in along-track direction within one scene (Breit et al., 2011). The residual phase noise, which comes from offsets in the relative oscillator and contributes to the relative height error in the derived DEM,

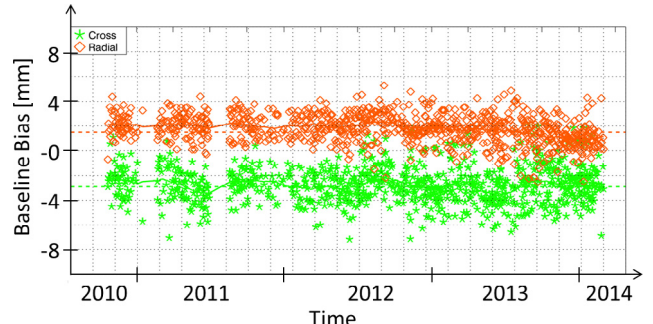


Fig. 2. Long-term evolution of the baseline bias: radial and cross-track components in red and green, respectively.

is thus reduced to the cm-level. Errors from rare events such as missing phase cycles or disturbances within the synchronization link might still be present and cannot be compensated for. For this reason, results are always compared to the bi-directional travel times (including individual instrument delays) of the compressed received pulses in the dynamically changing formation geometry (Breit et al., 2012; Krieger and De Zan, 2014). Detected deviations may trigger the reacquisition of individual data takes. The latter processing step is also necessary for synchronizing the timing of the passive satellite data to the active one. Otherwise, absolute geolocation and, specifically, radargrammetry of the passive image would be hampered by random errors of several cm in slant range.

- **Focusing, Bi-dynamic Geometry, and Geolocation:** The ITP focusing kernel is the one developed for the TerraSAR-X Multi-Mode SAR Processor (TMSP) (Breit et al., 2010b). Even for monostatic data, it does not use a stop-go approximation, but always a bi-dynamic approach to find the exact transmission time of a received echo, in order to determine the location of the antenna (s), the instantaneous orbit positions (and baselines), and zero-Doppler times for each acquisition sampling time.

In the TanDEM-X case, the mentioned parameters depend on the dynamically changing formation, on the local height of the illuminated ground area, and on the tropospheric and ionospheric delays in each part of the two-way signal path (Breit et al., 2010a). This bi-dynamic calculation provides image position dependent phase center locations in space and true range distances. It is performed iteratively on a grid and used consistently throughout the entire processing chain from focusing parameter generation to locally adaptive phase-to-height conversion within the geocoding process. While inaccuracies in these parameters would only lead to a minimal de-focusing, they are of utmost importance for accurate interpretation of topographic phase differences, leading to scene position and height dependent distortions in the order of several meters within a scene, if not properly considered. The implemented approach implicitly corrects for all absolute and relative ionospheric and tropospheric signal delays using a simple atmospheric model. The ITP kernel would theoretically be capable of providing the same centrimetric absolute geolocation accuracy of TMSP-products but it is limited in this respect since external weather and ionospheric maps and geodetic corrections are not operationally used (Balss et al., 2014). A horizontal absolute geolocation accuracy for the master image based on its absolute orbit in the sub-meter domain is sufficient for the 12 m resolution of RawDEMs where height errors (and the induced shifts) dominate. The main focus is now put on the relative geometric accuracy of the images provided by the two instruments, which is in the millimeter domain after applying the above corrections, thus comparable to the error in the baseline products.

- **Co-registration, Radargrammetry and Geocoding:** Having performed the steps above, the active and passive focused images are precisely matched in annotated timing and geometry. Nevertheless, the image contents obviously differ, mainly in range, due to the topography seen from the two parallactic viewing geometries. In order to match the same ground pixel for phase differencing, the two image signals have to be finely co-registered to achieve the maximum phase coherence resulting from interferometric filtering. This step is performed in the ITP with a threefold approach, which uses coherent cross correlation where possible and, as a fallback solution, incoherent cross correlation or coarse DEM based geometric prediction (Yague-Martinez et al., 2010). The approach is based on a trade-off between the capability to follow strong terrain changes in the high range-resolution data and the need for averaging over patches to yield accurate and consistent measurements for larger areas.

Properly co-registered images are a prerequisite for the computation of the interferometric coherence

$$\gamma = \frac{\mathbb{E}[u_1 u_2^*]}{\sqrt{\mathbb{E}[|u_1|^2] \mathbb{E}[|u_2|^2]}} \quad (1)$$

It represents the normalized correlation coefficient between master (u_1) and slave (u_2) acquisitions and quantifies the amount of noise which affects the interferogram (Bamler and Hartl, 1998). γ comprises all decorrelation sources such as signal-to-noise ratio, quantization, ambiguities, baseline decorrelation, volume decorrelation, and temporal decorrelation (Martone et al., 2012; Rizzoli et al., 2014). For extreme terrain and/or extreme baselines, coherence might be locally lost, resulting in an increase of the relative height error in mountainous terrain. Hence an outlier rejection and interpolation scheme is applied to minimize these effects. For operational TanDEM-X DEM acquisitions, the size of the coherence estimation window is set to 11 pixels \times 11 pixels in azimuth and range dimensions, which grants an almost unbiased coherence estimate (Touzi et al., 1999).

Since the (local) bi-dynamic baselines, the timing synchronization and the focusing geometry are precisely known, all residual image shifts, measured in the process above, are considered to be the true topographic signal. Unlike other interferometric processors, the ITP does not correct for assumed baseline/orbit-errors from measured cross-correlation image shifts but uses this information to generate a stereo-radargrammetric absolute phase which provides the absolute height of the patches (Rossi et al., 2012). This measurement is limited in its accuracy by the small parallactic angles of the nominal TanDEM-X formation. Again, an outlier rejection and averaging scheme is therefore applied. The main output of this step is the absolute integer phase offset cycle for the entire scene which is added to the relative measurement of the unwrapped interferometric phases. The ITP provides geocoded RawDEMs where any error in this absolute phase offset would correspond to height errors of an integer multiple of the height of ambiguity h_{amb} . The latter is defined as the height difference equivalent to a complete 2π phase cycle in the interferogram and, for the bistatic case, can be expressed as

$$h_{\text{amb}} = \frac{\lambda r \sin(\theta_i)}{B_{\perp}}, \quad (2)$$

where λ is the radar wavelength, r the slant range, θ_i the incidence angle, and B_{\perp} the perpendicular baseline.

This height offset can be easily corrected during the final DEM calibration; nevertheless, it also has an implication on the horizontal accuracy of the geocoded DEM, causing a (range) shift in the

same order of magnitude plus a tilt and, to a much less extent, to the height dependent tropospheric correction applied. Using radargrammetry it is possible to position the interferogram in the correct 2π phase ambiguity band. As already mentioned in the previous paragraph about synchronization, the bistatic system also showed π -ambiguities in the phases from the synchronization link between the two satellites, which occurred in about 10% of the cases and were corrected by re-processing in a feedback loop with the subsequent calibration processor.

Geocoding is therefore an active process which locates and also connects samples in 3D according to their phase information. Areas without coherent phase information (i.e. layover regions; (Rossi et al., 2014)) are thus interpolated (in range) and identified by the maximum height error in the corresponding mask. Nominally, the RawDEMs do not contain intrinsic invalid data: each sample inside the scene is set to a valid value. This includes (random) height data for the incoherent areas like water bodies or radar shadows. There are exceptions where larger areas of incoherent data are identified with the help of global water masks, derived from the GLOBCOVER land classification map (GLOBCOVER, 2015), and replaced by an arbitrary, but consistent, simulated phase information to avoid errors from artificial phase trends in unwrapping these large scale water bodies. A similar method is applied in phase unwrapping correction to temporally inconsistent areas. This process is called phase modification and the data are flagged accordingly in the RawDEMs as invalid when considered for the mosaicking.

If correctly unwrapped (and reprocessed, if required), the ITP thus delivers RawDEMs which are accurate in height and associated location to an error corresponding to the 1–2 mm cross-track baseline error and, in addition, the residual phase errors from synchronization and processing approximation in the equivalent mm range. All the above phase and range delay errors have to be scaled with the height of ambiguity, eventually yielding 1–3 m absolute height errors before final calibration for nominal interferometric acquisitions.

2.4. DEM error sources

Several error contributions may affect the quality of an interferometric SAR (InSAR) DEM; they depend on both the particular land cover and terrain characteristics of the area under illumination and the specific acquisition geometry used for the data take. They are shortly summarized in the following paragraphs:

- **High-relief terrain:** SAR acquisitions over steep and irregular surfaces are often affected by geometric distortions, such as shadow and layover. The first occurs when target areas are behind a mountain ridge and are therefore not illuminated by the radar wave, the second occurs if objects at different heights are imaged into the same resolution cell, hence interfering with each other. In both cases a gap in the data (no information) is observed. In most cases a re-acquisition of the affected area from a different orbit position mitigates such effects, as shown in Fig. 3. The combination of two TanDEM-X acquisitions acquired in ascending and descending viewing geometry allows for gap closure for 70% of the affected areas. For the remaining ones, additional acquisitions with steeper incidence angles are currently being acquired, for eventually perform a DEM update in the future.
- **Forested areas:** Over vegetated areas the presence of multiple scatterers at different canopy heights within a single resolution cell results in an increase of the interferometric phase uncertainty (Treuhaut and Siqueira, 2000). X-band radar waves are characterized by a limited penetration capability, and volume decorrelation phenomena over densely forested areas strongly

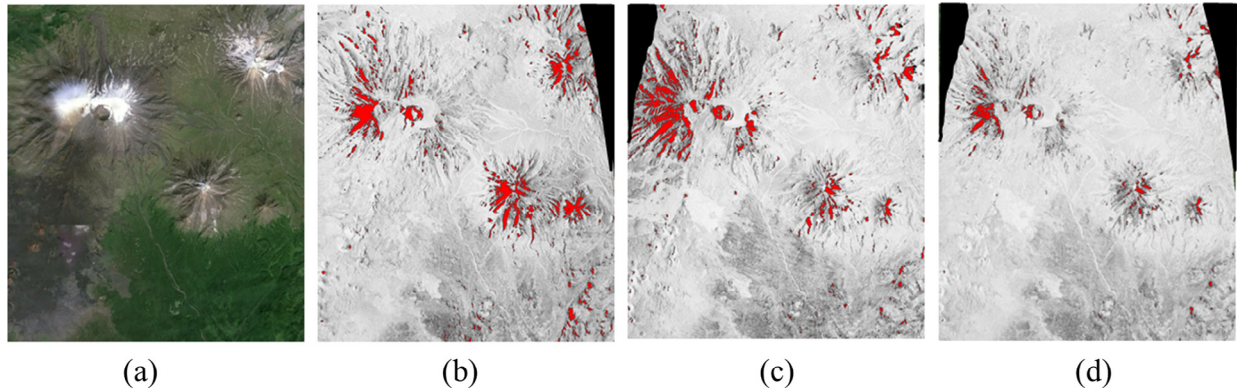


Fig. 3. (a) Optical image of three up to 3700 m high volcanoes in Kamtchatka. Coherence maps of two TanDEM-X acquisitions acquired in ascending (b) and descending (c) viewing geometry, respectively. In each image pixels affected by either shadow or layover (due to very steep slopes) are indicated in red. By combining the two acquisitions, about 70% of the affected areas can be correctly resolved, as shown in (d).

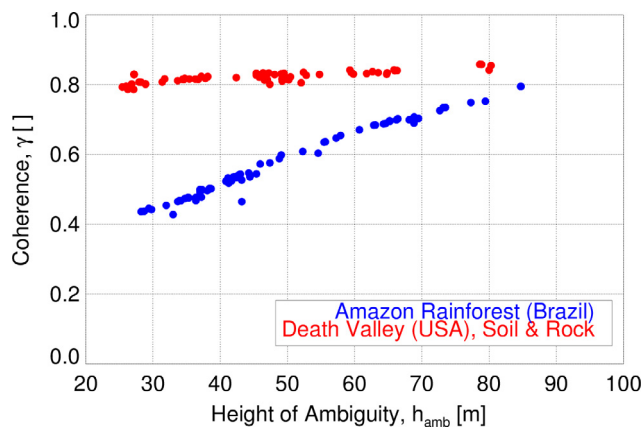


Fig. 4. Interferometric coherence over height of ambiguity h_{amb} : for the Death Valley test site (in red) almost no influence of the baseline on the coherence is observed; on the other hand, for densely forested areas (in blue) volume decorrelation strongly depends on the imaging geometry.

depend on the specific acquisition geometry (Martone et al., 2012). As an example, the mean interferometric coherence per image for two test areas, characterized by different land covers, is shown in Fig. 4, as a function of the height of ambiguity h_{amb} . Since early in the mission these two test sites have been repeatedly acquired with varying Helix formations for long-term monitoring of the interferometric performance. The Death Valley test site (red dots) is characterized by a non-vegetated, rocky land cover. It shows a substantial stability of the interferometric coherence over the height of ambiguity (for this land cover type, the main source of coherence loss is the limited SNR). On the other hand, the Amazon rainforest test site is covered by dense forest where volume scattering takes place and the coherence is clearly increasing with increasing height of ambiguity. An optimized acquisition geometry, using smaller baselines (i.e. larger h_{amb}), mitigates the decorrelation effects due to volume scattering and hence improves the quality of the phase-unwrapping process, resulting in a higher DEM quality.

- **Snow and ice:** Analogous to vegetated areas, dry snow/ice regions are also characterized by volume scattering, which leads to volume decorrelation and contributes to a degradation of the interferometric performance. Depending on the snow properties, X-band radar waves may be able to penetrate up to 10 m below the ice surface (Rizzoli et al., 2017). For this reason, together with smaller-baseline re-acquisition (as done for

forested regions), over vast snow-covered areas, such as Greenland or Antarctica, a dedicated calibration approach of the DEM has been developed, as later presented in Section 2.6. A more detailed analysis of volume decorrelation effects over forested and ice covered regions is discussed in Martone et al. (2016b).

- **Sandy deserts:** The quality of SAR surveys over sandy regions is strongly affected by the weak backscattered returns. For the nominal TanDEM-X incidence angles range between 30° and 48° the low SNR is the main error source degrading the InSAR performance (Martone et al., 2016a). Steeper incidence angles result in an increased backscatter, as shown in Fig. 5 for two bistatic scenes over the Sahara desert in Egypt at incidence angles of 17° and 37°. The 10 dB increase in SNR doubles the coherence.

• **Phase unwrapping errors:** The most prominent errors in the interferometric DEM processing are phase unwrapping errors. The interferometric phase measurement is ambiguous within 2π and the phase of every height difference exceeding the height of ambiguity h_{amb} is wrapped into the baseband. The process of phase unwrapping (PU) reconstructs the absolute, continuous phase from the wrapped data by adding the correct integer 2π cycle number to the wrapped values. The ITP uses a Minimum Cost Flow (MCF) approach to find consistent phase cycles weighted by the interferometric coherence (Lachaise et al., 2014b). This approach is reliable as long as the continuity of the signal is given. In cases where regions of different height are separated by regions of incoherent data or if the interferometric phases show significant jumps in the order of the height of ambiguity, a correct unwrapping is not possible without additional information. Such discontinuities can be caused by forest edges, water bodies or shadow and layover regions. The resulting DEM exhibits erroneous regions with height offsets corresponding to multiples of the (local) height of ambiguity. Due to the side-looking viewing geometry, they are also displaced in range roughly by the same distance.

In TanDEM-X, the very small height of ambiguities needed to achieve the low relative height errors are prone to these errors. Larger errors can be detected from discrepancies between the stereo-radargrammetric phase and the unwrapped phase, but the radargrammetric information is too coarse for a correction. Therefore a sophisticated algorithm has been developed and implemented in the ITP which combines at least two acquisitions with different baselines from the same viewing geometry to locally solve the ambiguities (Lachaise et al., 2014a).

A pre-requisite for successful unwrapping is a ratio of the two heights of ambiguity of approx. 0.7, temporally stable and coherent topography, and a minimum size of several km² of

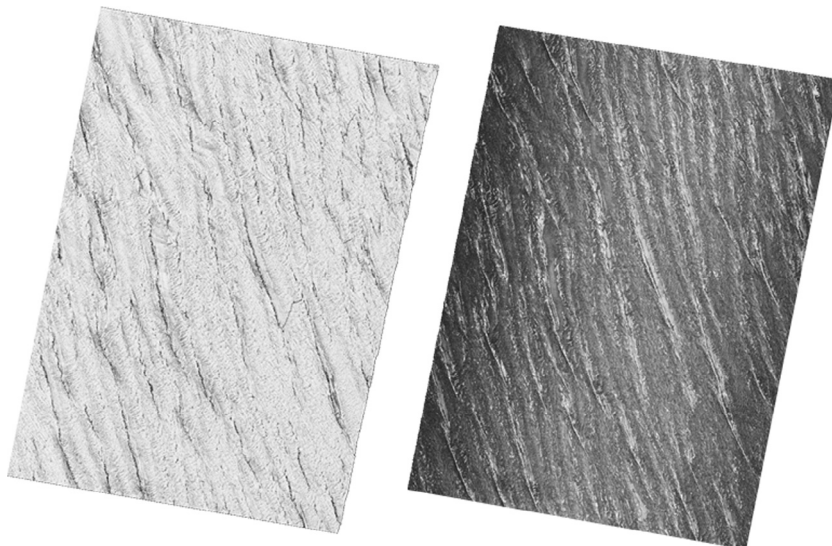


Fig. 5. Interferometric coherence of two TanDEM-X bistatic scenes over the Sahara desert in Egypt. For the image on the left-hand side, the acquisition mean incidence angle is 17° , for the one on the right-hand side it is 37° . The SNR is around 10 dB higher in the left image, and a coherence improvement of about 90% (from 0.44 to 0.83) is obtained.

the discrepant area. Under these conditions, the algorithm has a success rate of about 97% in correcting larger errors. The challenges with temporal changes and different height of ambiguity ratios in TanDEM-X data are outlined in (Lachaise et al., 2014b). If errors are detected but cannot be corrected or a scene is not covered with a matching acquisition at the time of processing, the corresponding parts of the generated RawDEM are invalidated. In rare cases this leads to gaps in the final DEM. Smaller PU errors specifically persist in incoherent areas (e.g. forests). These errors are mostly solved in the mosaicking process by grouping together consistent heights from different RawDEMs, as detailed in Section 2.6.

2.5. Acquisition strategy and acquisition parameters optimization

The acquisition strategy for the generation of the global DEM is driven by the mission specification on the relative height accuracy (see Table 1), which is in turn directly related to the height of ambiguity h_{amb} . Hence, h_{amb} needs on one hand to be sufficiently small to guarantee the fulfillment of the global mission specification and, on the other hand it has to be large enough to guarantee a robust phase unwrapping process.

Nominal DEM acquisitions were performed in right-looking observation mode, in ascending orbits over the Northern hemisphere, and in descending orbits over the Southern one. In order to prevent the satellites from irradiating and potentially damage each other, so-called exclusion zones have been defined, which constrain the portions of the orbit in which each satellite can be active or passive for bistatic data takes.

In the first year of operation, from December 2010 to March 2012, a global acquisition of the Earth's landmasses, excluding Antarctica, was carried out. According to the acquisition strategy, the orbit formation was properly set in order to keep a h_{amb} of about 50 m for all different incidence angles and latitudes. In Fig. 6 the evolution of the flight formation parameters, i.e. horizontal and vertical baseline, and of the height of ambiguity (represented by the blue and red line, and by the grey circles, respectively), are depicted as a function of time for the entire mission duration. The Helix formation has been continuously reconfigured to achieve different goals. As an example, in April 2011, the minimal h_{amb} was increased from 40 m to 45 m in order to mitigate

strong volume decorrelation phenomena over forested areas. To allow reliable phase unwrapping, additional acquisitions were performed over densely forested areas (e.g. over the Amazon rain forest in Brazil or the tropical forest in South East Asia) and over mountainous regions as well. For this reason, acquisitions with h_{amb} typically larger than 60 m, hence requiring smaller baselines, were commanded. Such acquisitions were performed starting from October 2011 (the corresponding h_{amb} also indicates a larger variation in Fig. 6).

The acquisitions of the second global coverage started in April 2012 and lasted until April 2013. The target h_{amb} was reduced from 50 m to 35 m. The decrease in h_{amb} by a factor of 0.7 has been found to be optimal in order to combine the two acquisitions for the exploitation of multi-baseline phase unwrapping algorithms and for the overall improvement of the relative height accuracy, as already described in Section 2.4. Additionally, the two global coverages have been performed by using slightly mutually displaced elevation antenna beams to keep the final performance almost uniform over the slant range dimension. In this way it never occurs that a target on ground is illuminated at the beam's borders in both coverages, which are characterized by lower SNR with respect to the beam center. The transition to the second year of acquisition is clearly visible in Fig. 6 in the sudden jump of the formation and in a consequent decrease of h_{amb} .

Continuous performance analysis and monitoring during the first two years suggested the need to perform further acquisitions with optimized imaging geometry over critical areas. Referring to the global coherence map of the first year shown in Fig. 7, one can notice reduced coherence values over forested area, as well as over snow- and ice-covered ones, deserts, and mountainous regions (see also Section 2.4). Dedicated acquisition strategies have been applied, as shortly illustrated in the following.

In order to cope with weak backscatter returns from sand, deserts have been reacquired between August 2013 and February 2014 with steeper incidence angles (between 14° and 27°) to improve the interferometric performance. During the same time period, mountainous regions have been reacquired as well. The occurrence of geometrical distortions, such as shadow and layover, suggested the need of reacquiring such areas from an opposite viewing geometry. Therefore, the Helix configuration has been accordingly adapted to perform acquisitions in descending orbit

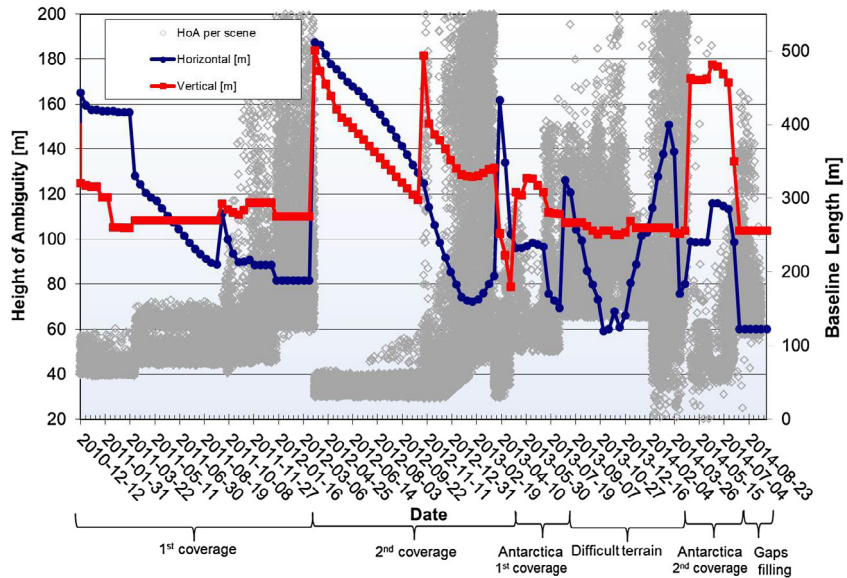


Fig. 6. Evolution of the flight formation parameters over the full mission time and corresponding height of ambiguity h_{amb} (gray) for the global TanDEM-X DEM acquisition. The vertical baseline is shown in red, while the horizontal one in blue.

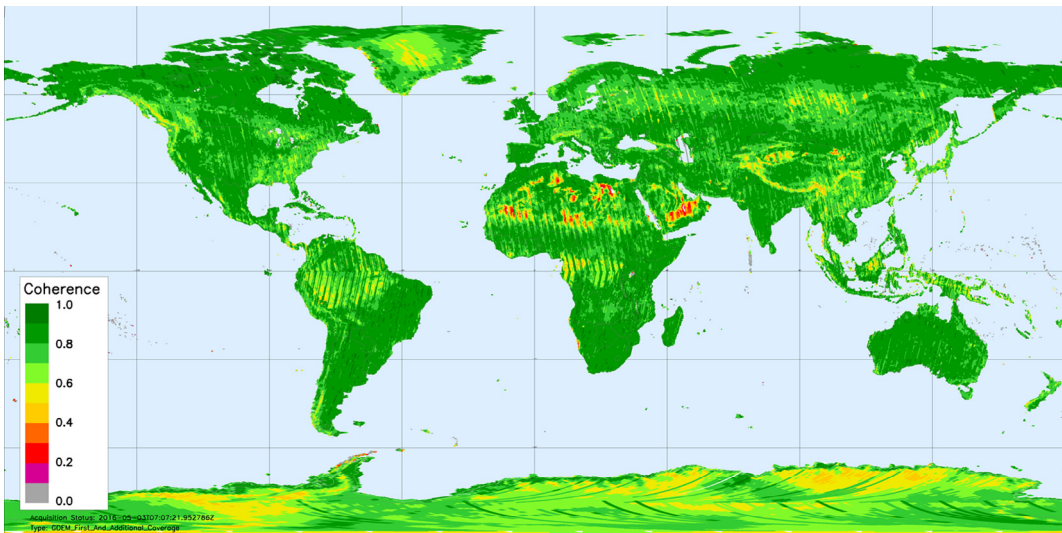


Fig. 7. Global interferometric coherence estimated from the acquisitions of the first TanDEM-X coverage.

direction in the Northern hemisphere and in ascending direction in the Southern one (Borla Tridon et al., 2013). In addition, during this time period, a minimum horizontal distance between the two satellites of 120 m has been set in order to reach a sufficiently large h_{amb} (above 60 m). In Fig. 6 one can notice the described change in the formation parameters. From August to November 2013 the vertical and horizontal distances progressively decreased, and increased then again until February 2014 (Borla Tridon et al., 2013; Maurer et al., 2014). In this way two independent sets of acquisitions have been performed, to further increase the resulting DEM accuracy. To complete the global DEM generation, Antarctica has also been acquired twice: during the austral winter, between May and July 2013, and during the same months in 2014. This allowed to obtain a stable performance since no significant snow melt occurs. Due to the inclination of the TerraSAR-X and TanDEM-X satellite orbits, the central part of Antarctica (over a radius of 1300 km from the South Pole) cannot be seen in the nominal right-looking imaging mode. For this reason, left-looking

observations, using shallower incidence angles above 50°, were required. However, this leads to several additional challenges: indeed, due to their inclination, the satellites experienced an eclipse during this period, which affected the charging capability of the on-board batteries. In addition, in left-looking mode, the intake on the solar panels is lower than in right-looking mode as the satellites are rotated away from the sun.

On the TerraSAR-X and TanDEM-X satellites, the received backscattered signal is first digitized by an 8-bit analog-to-digital converter (ADC) and then further compressed by a block adaptive quantizer (BAQ). For nominal mission operation, mostly BAQ quantization with 3 bits for both satellites has been commanded, representing a good compromise between data volume and resulting product quality (Martone et al., 2015). Compression rates up to 2 bit/sample have been selected for areas showing very good performance as well as homogeneous backscatter characteristics to further increase the orbit time availability for re-acquisition of affected data, without impacting (but rather

improving) the overall mission performance (Martone et al., 2015).

Furthermore, several factors may lead to bad DEM data quality or missing data and trigger an acquisition rescheduling, such as:

- interferences in the data caused by radar systems for air control, military or weather forecast, or even by other spaceborne SAR sensors,
- severe meteorological events leading to a distorted phase information and unreliable height estimation,
- inappropriate height of ambiguity or season of acquisition due to shifting of the acquisitions may lead to a bad data quality for phase unwrapping (see Section 2.6),
- loss of data during the downlink caused by meteorological effects as well as contingencies during data transfer to the on-ground processing facilities,
- conflicts with commercial acquisitions of the TerraSAR-X mission (Schättler et al., 2015; Zink and Buckreuss, 2015).

Due to the occurrence of the above listed issues and problems, about 5% of the around 60,000 acquisitions were impacted by one of these issues and needed to be rescheduled. The total amount of coverages acquired for the global DEM is shown in Fig. 8. The red swaths indicate acquisitions over rather flat terrain that needed to be re-planned. Most the land masses were covered by two interferometric acquisitions (green).

2.6. Global DEM generation process: from single scenes to DEM mosaic

As described in Section 2.3, the ITP uses no external reference data for height calibration or phase unwrapping (Fritz et al., 2011). It relies solely on the excellent synchronization, baseline accuracy, and delay and phase calibration of the TanDEM-X system for DEM geocoding. The small remaining offsets and tilts for a single data take are in the range of few meters (most of them are even below ± 2 m), see Fig. 9.

These residual errors are estimated and compensated in the subsequent TanDEM-X DEM Mosaicking and Calibration Processor (MCP), whose main processing steps are summarized in the following:

1. The first step of the MCP processor comprises a data-driven analysis of the input DEM scenes provided by the ITP processor, performed by the so-called DEM Preparation Processor. In par-

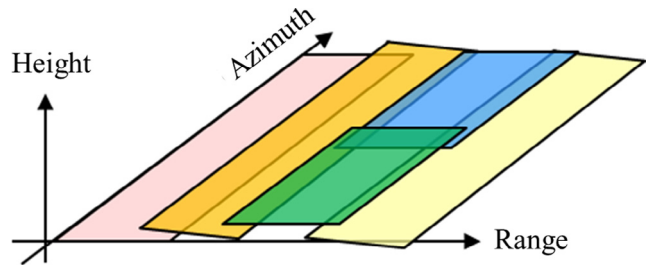


Fig. 9. Data takes with individual residual offsets and tilts in range and azimuth.

ticular, it aims to detect phase unwrapping errors by comparison with overlapping DEM scenes and reference data, e.g. SRTM C-band or GLOBE. Moreover, tie points and ground control points (GCPs) are extracted for the proper DEM calibration step. Tie-points connect adjacent DEM acquisitions in the approximately 4 km-overlap-area with each other (see Fig. 9) and consist of equidistantly spaced areas (approximately every 1 km in azimuth) of the same size of an ICESat footprint (around 70 m of diameter) (Huber et al., 2010).

2. In a second step, all DEM scenes, where phase unwrapping errors are detected, are reprocessed by the ITP processor. Primarily, DEM scenes from the first coverage and processed with single-baseline unwrapping are unwrapped again using dual-baseline techniques, if adequate coverages are available (Lachaise et al., 2012).
3. In the third step, all DEM scenes are calibrated and adjusted to each other and to the available ground control points (Hueso Gonzalez et al., 2010a; Hueso Gonzalez et al., 2012). The latter is performed by a block adjustment procedure using a least-squares approach within the DEM Calibration Processor (Gruber et al., 2016). The global available ICESat (Ice, Cloud and land Elevation Satellite) data, introduced in the next paragraph, is used as reference data set for absolute ground control.
4. In the fourth step, all DEM scenes are fused together within the DEM Mosaicking Processor, by applying an optimized logic which seeks to minimize residual phase unwrapping errors (Gruber et al., 2012).

The reference ICESat data set and the last two steps are described in more detail in the following subsections.

ICESat Elevation Data. The ICESat spaceborne laser altimeter data is a unique data set that provides globally distributed, accu-

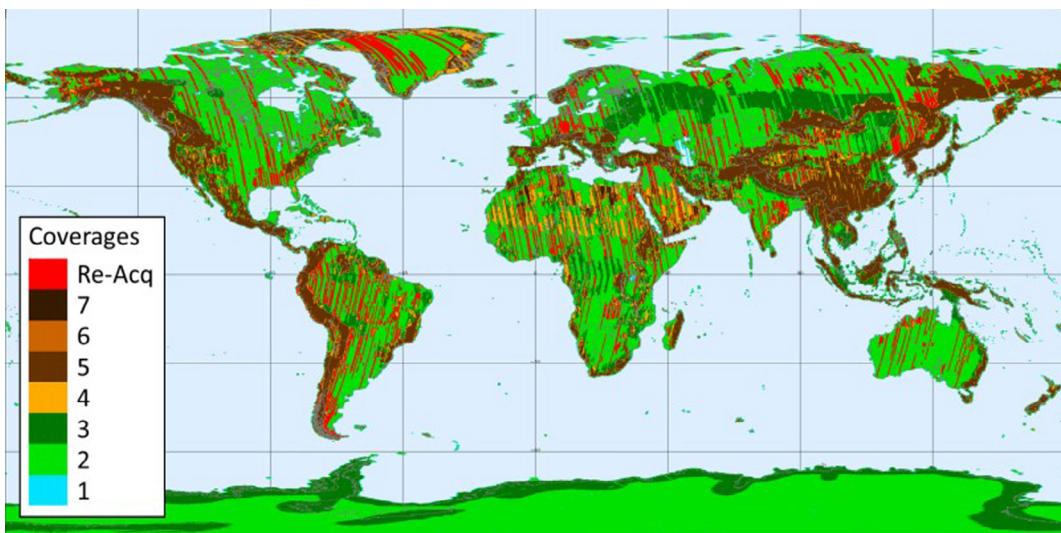


Fig. 8. Amount of coverages acquired for the global DEM including re-acquisitions.

rate height information, as well as performance evaluation and classification information for each provided measurement point (Schutz et al., 2005). The specific data set used for supporting the TanDEM-X mission is the *GLAS/ICESat L2 Global Land Surface Altimetry Data, Version 34, GLA14* (Zwally et al., 2009). A global coverage is provided by illuminating the ground using a 70 m footprint at a point distance of 170 m in along-track and a maximum point distance of 80 km in across-track direction. In order to ensure the good height accuracy of ICESat points used for TanDEM-X DEM calibration, several selection criteria are considered, extracting only the most reliable ones (Hueso Gonzalez et al., 2010b). Criteria like number of peaks of the reflected signal (indicator for vegetation), received energy and signal range (indicator for terrain) are applied. Outliers above 100 m compared to TanDEM-X DEM scenes are eliminated. According to a previous accuracy study, the standard deviation for these selected GCPs is below 2 m under optimal conditions (ICESat points on flat bare land) (Huber et al., 2009). Therefore, the selected ICESat GCPs are well suited to achieve the aimed accuracy of 10 m absolute height error. In order to combine ICESat points and the corresponding TanDEM-X pixels, all elevation values provided by TanDEM-X within a single ICESat footprint are averaged, according to a laser specific weighting function (Harding and Carabajal, 2005). As calibration points (CGCPs) for the block adjustment, in general only the best 10 ICESat points per the 50 km long DEM scene are used. In total, just a small subset of selected ICESat points is used for calibration, and a much higher number is used as validation ground control points (VGCPs) for the final DEM heights, as explained in Section 3.1. In addition, for validation points the standard deviation of the TanDEM-X DEM scene within the footprint must be below 1 m.

Block adjustment of DEM acquisitions. For each data take, correction parameters like height offset, tilts in the slant range dimension, and slopes in the azimuth one are derived by means of a weighted least-squares adjustment. The DEM adjustment was simplified by reducing the number of unknowns, i.e. the number of DEM data takes (Gruber et al., 2012). Therefore, long data takes, on average about 700 km, were acquired. ICESat points are used as GCPs to adjust the TanDEM-X DEM to fixed values. Furthermore, tie points located within the 3 km of range overlap between two independent acquisitions are used to derive height differences between tie points. These tie points are in reality tie point areas with a size of approximately 1 km × 1 km. They are equidistantly

spaced along the overlap azimuth center line, and can be exploited for DEM block adjustment. Since the adjusted heights $\hat{H}_{i,j}$ and $\hat{H}_{i,k}$ of two measured heights $H_{i,j}$ and $H_{i,k}$ of data take J and K of a tie point should be identical, apart from a residual random noise, such a condition can be written as

$$\hat{H}_{i,j} + \hat{v}_j = \hat{H}_{i,k} + \hat{v}_k, \quad (3)$$

As the adjusted observations has to follow the form $\hat{L}(\phi(\hat{x})) = 0$ to be introduced into the weighted least-squares adjustment (Niemeier, 2002), this term can also be written in the form

$$[H_{i,j} + g_j(\hat{x})] - [H_{i,k} + g_k(\hat{x})] + \hat{v}_i = 0, \quad (4)$$

where $H_{i,j}$ and $H_{i,k}$ are the observed heights, $g_j(\hat{x})$ and $g_k(\hat{x})$ are the error functions with the adjusted correction parameters $\hat{x} = [a \ b \ c]$: offset a , tilt in range direction b , and slope in the azimuth direction c , and \hat{v}_i are the summarized residuals. The advantage of this method is that the correction parameters can be found independently from terrain types. As the DEM data acquisitions followed the global scenario presented in Section 2.5, a dedicated DEM calibration of larger blocks is triggered when all overlapping acquisitions for such an area are available.

Greenland and Antarctica Calibration. X-band radar waves are able to penetrate a snow pack by several meters depending on the snow micro-structure, its dielectric properties, and the acquisition parameters, such as frequency and incidence angle (Benson, 1962, Reprinted Aug. 1996; Weber Hoen and Zebker, 2000). Hence, the resulting interferometric SAR measurements represent the surface elevation corresponding to the mean phase center of the backscattered signal. Special adaptations to the nominal TanDEM-X DEM calibration are conducted to maintain these characteristics for both Greenland and Antarctica, avoiding an artificial raise or even deformation of the resulting DEM upwards to the ground control points. The largest penetration depth occur in presence of dry snow, which characterizes e.g. the inner part of Greenland and almost entirely the Antarctic continent (Rott et al., 1993). On the other hand, at the outer coastal regions of Greenland, mostly characterized by steeper bare areas, surface scattering predominates. In this case, the radar height estimate using interferometry matches quite well with the one retrieved from ICESat GCPs.

Based on these concepts, two different strategies have been developed for calibrating Greenland and Antarctica:

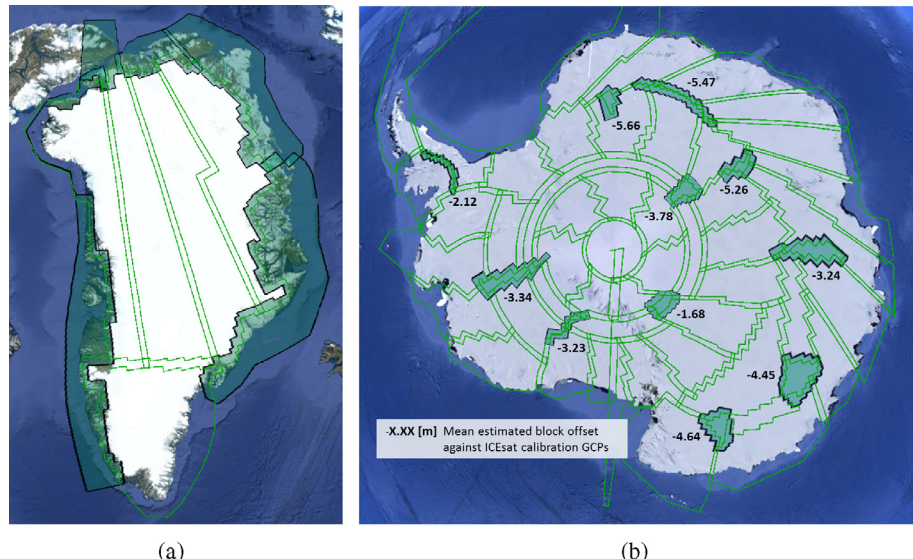


Fig. 10. DEM Calibration blocks for (a) Greenland and (b) Antarctica. For Greenland solely the outer, greenish blocks where adjusted to GCPs. For Antarctica, the filled green blocks were calibrated using the mean difference to ICESat GCPs, in order to maintain the measured mean SAR penetration depth.

- For the block adjustment of Greenland, ICESat elevation measurements exclusively over the outer coastal regions are used as GCPs (Wessel et al., 2016). In the inner ice sheet regions, the TanDEM-X DEM calibration of Greenland solely relies on tie points within the overlapping regions and data are accordingly calibrated following a *outer-to-inner* direction. The different blocks, calibrated on GCPs and tie points only, are depicted in Fig. 10a.
- Antarctica covers an area which is too extended to be able to be adjusted within one single free-adjustment only. Moreover, not enough zones without snow and ice cover are available for calibration using ICESat GCPs according to the Greenland calibration concept. Therefore, as reference heights to be compared to ICESat points, areas characterized by homogeneous backscattering characteristics and therefore predominantly homogeneous penetration depths are chosen. These areas were manually selected with the help of the Radarsat-1 Antarctica amplitude mosaic (Jezek, 2002) and are displayed in Fig. 10(b) (green blocks). They are located in the inner Antarctic continent, kilometers away from the shelf ice tide-induced coast. For each of these fixed blocks the mean height difference between the TanDEM-X and ICESat elevation information is calculated and

applied as a constant bias, referring the entire block to a mean InSAR height below the surface. Starting from these fixed blocks, all other Antarctica acquisitions are adjusted solely relying on tie points and on the already calibrated areas, as done for the Greenland's inner areas.

Mosaicking of Multiple TanDEM-X DEMs. During the mosaicking process, the estimated calibration corrections are applied to each single input DEM scene and different coverages are mosaicked together by evaluating a weighted average of the K available elevation values. For the i^{th} output pixel, the mosaicked height h_i is obtained as:

$$h_i = \frac{\sum_{k=1}^K \frac{1}{\sigma_{HE,k}^2} h_k}{\sum_{k=1}^K \frac{1}{\sigma_{HE,k}^2}} \quad (5)$$

where, for a certain input elevation h_k , the corresponding weight is derived from its relative height error standard deviation estimate $\sigma_{HE,k}$, obtained from the interferometric coherence as presented in Section 3.2. Beside this widely used mosaicking approach, one big challenge remains the handling of larger height discrepancies

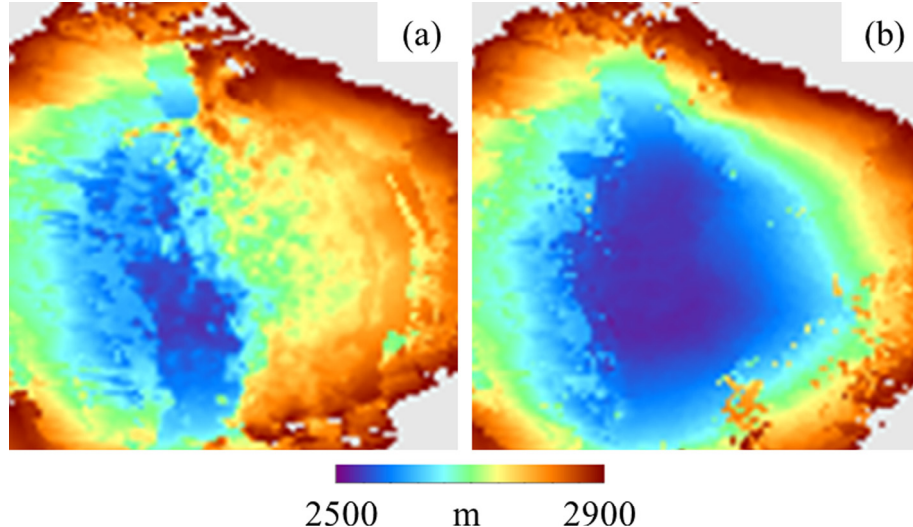


Fig. 11. Volcanic crater in the region of Kamtchatka. (a) DEM mosaic using a pure weighted mean, (b) DEM mosaic with a weighted mean of the most reliable height group according to InSAR quality parameters. The different height values between (a) and (b) are due to temporal changes.

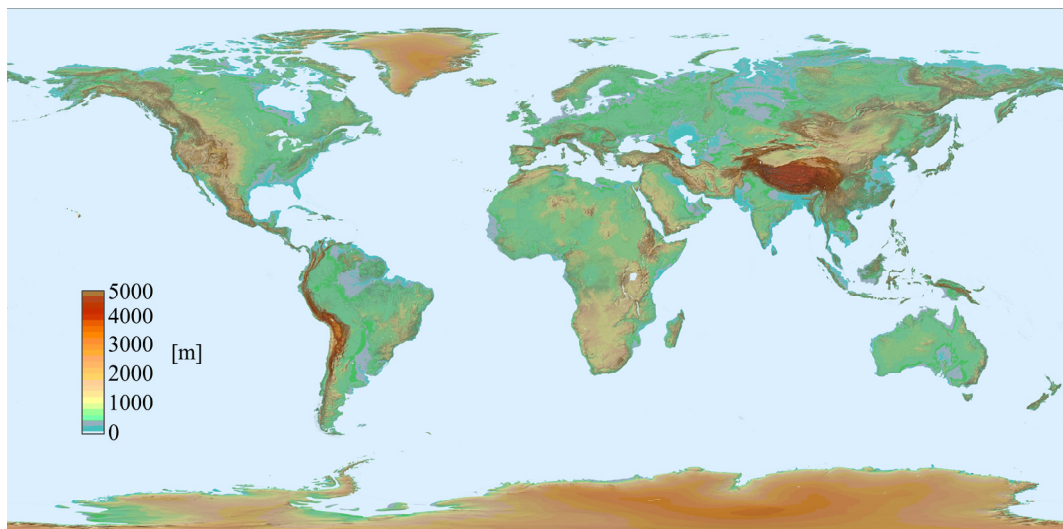


Fig. 12. Overview of the global TanDEM-X DEM.

among the input data, which are mainly caused by phase unwrapping errors or by height changes between different acquisitions. In case of such inconsistencies, the TanDEM-X mosaicking approach performs a first grouping of all input height measurements into several height intervals. A priority concept is set up to evaluate the reliability of different groups of heights, considering the number of available DEMs and several InSAR quality parameters, such as the relative height error estimate, the applied phase unwrapping method, and the height of ambiguity of the original acquisitions (Gruber et al., 2012). This allows for the identification of the most reliable height interval to be used for mosaicking. As an example, one can consider the volcanic crater in the region of Kamtchatka, displayed in Fig. 11: the DEM mosaic with a weighted mean of all input height measurements Fig. 11a and the weighted mean within the best height interval Fig. 11b which is much less noisy than the one generated by applying the weighted mean on all available height estimates.

Finally, after the complete DEM mosaicking process, the resulting DEM geocells are subject to an interactive quality control.

The Global TanDEM-X DEM Product. The global TanDEM-X DEM is partitioned into geocells, whose size is latitude dependent ($1^\circ \times 1^\circ$ in latitude/longitude between $\pm 60^\circ$, $1^\circ \times 2^\circ$ between $\pm 60^\circ$ and $\pm 80^\circ$, and $1^\circ \times 4^\circ$ between $\pm 80^\circ$ and $\pm 90^\circ$) each of which can be individually accessed by the users. Each single product consists of various layers which provide the user with the combination of the height measurements and corresponding additional information. Furthermore, a metadata file is provided, which includes among other things, the acquisition dates of the individual acquisitions contributing to a specific geocell. Aside from the DEM itself, the seven additional information layers provided for each geocell are (Wessel, 2016):

- height error map (HEM),
- mosaic of the mean amplitude (AMP),
- mosaic of the minimum amplitude (AMP2),
- water indication mask (WAM),
- coverage map (COV),
- consistency mask (COM),
- layover and shadow mask (LSM).

It should be noted that the values of the height error map (HEM) correspond to height errors caused by random noise contributions and are in form of standard deviations. The mosaicked HEM is eval-

uated by averaging single HEM values from the input scenes, which are derived from the interferometric coherence and geometrical considerations (Wessel, 2016), and represents the result of a rigorous propagation of errors in both the interferometric phase determination and in the combination of different coverages.

An overview of the global TanDEM-X DEM is presented in Fig. 12. Overall, a total amount of over 470,000 DEM scenes each with a ground extension of about $30\text{ km} \times 50\text{ km}$ has been used for the generation of the global TanDEM-X DEM mosaic. Including all processing and re-processing iterations, more than 600,000 scenes were processed. As an example, the MCP processor has processed up to 4 Terabytes of data each day.

The global TanDEM-X DEM is an unedited DEM created from SAR interferometry only, e.g. open water surfaces will show a noisy relief due to low coherence and/or low backscatter. Depending on the application, subsequent DEM editing like flattening of water bodies or void interpolation might be necessary. The Water Indication Mask (WAM) could provide a supplementary information layer to support such a process.

3. Global DEM performance

In this section the global accuracy of the TanDEM-X DEM is assessed in terms of vertical absolute and relative height accuracy (Sections 3.1 and 3.2, respectively), and coverage statistics (Section 3.3).

The fourth parameter in Table 1 to be assessed is the horizontal accuracy of the final DEM, which is directly related to the geolocation accuracy of the input scenes to be mosaicked (Balss et al., 2014). It represents a fundamental quality descriptor for the ITP processing chain, and has been already addressed in Section 2.3, hence it will not be discussed further.

The performance presented in this section is assessed for three different classes of DEM geocells separately, according to the dominant land cover type:

- forest geocells: characterized by more than 60% of forest coverage, where the presence of forest is detected by using a weighted combination of the GLOBCOVER 2010 classification map (GLOBCOVER, 2015) and PALSAR forest/non-forest map (Shimada et al., 2014).

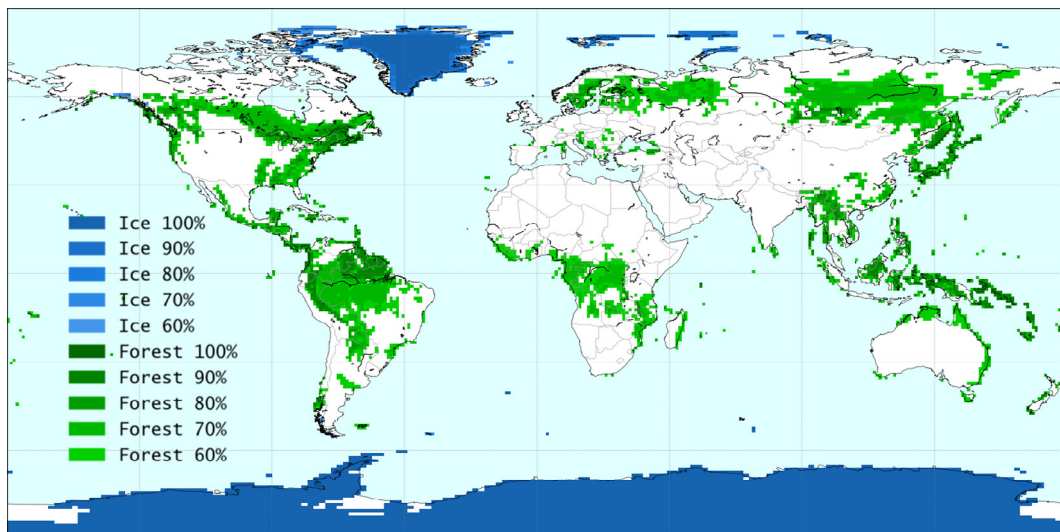


Fig. 13. Distribution of DEM geocells identified as *forest* (green) and *ice* (blue) using a combination of GLOBCOVER 2010 classification map (GLOBCOVER, 2015) and PALSAR forest map (Shimada et al., 2014).

- *ice geocells*: characterized by more than 60% of ice or snow coverage, where the presence of ice or snow is detected using the GLOBCOVER 2010 classification map. For the absolute height accuracy analysis, the entire Antarctic landmass is included in this category.
- *generic geocells*: all other geocells, only marginally affected by volume decorrelation.

The global distribution of *Forest* and *Ice* geocells is depicted in Fig. 13.

3.1. Absolute height accuracy

The absolute vertical accuracy represents the uncertainty in the height of a point with respect to the WGS84 ellipsoid caused by uncorrected, slow-changing systematic errors (see Section 2.1). The evaluation of the final TanDEM-X DEM performance is based on the difference between TanDEM-X and ICESat elevation data, as detailed in the following.

Evaluation Method. The absolute vertical accuracy of the TanDEM-X DEM data is validated with the globally available elevation data provided by ICESat. It is of course a compromise to compare two different sensors, characterized by different technologies and resolutions, however such an approach was evaluated to be the best practical solution for assessing the TanDEM-X DEM abso-

lute height accuracy performance at a global scale. The ICESat data set was chosen as global validation data set because of its vertical accuracy of better than 1 m, which ensures a sufficient precision for a consistent validation (Zwally et al., 2009), as well as its global coverage.

The illumination characteristics of the laser-based ICESat system differ from the radar-based TanDEM-X one. This difference becomes noticeable over regions covered by forests or snow/ice. In the case of snow/ice, for example, the radar wave penetrates into the snow pack, leading to volume scattering mechanisms, whereas the laser pulses are effectively reflected by the top of the reflecting snow surface, increasing the differences in height estimates between the two systems.

To evaluate the absolute height accuracy on a global scale, for each DEM geocell the 1000 ICESat points, showing the lowest TanDEM-X height variation within the ICESat footprint, are considered. This approach aims to assure that the majority of geocells are validated with a comparable number of validation points. With this approach mainly flat regions are considered for the comparison, since they are characterized by the lowest spatial variance. The prioritization of flat regions in the evaluation does not compromise the validity of the proposed method, as the main error sources are the remaining tilts and low-varying trends, which affect the entire geocell.

An example from Madagascar of ICESat tracks as well as demonstrating TanDEM-X DEM geocells with uneven ICESat point distributions, is shown in Fig. 14. It is worth pointing out that the subset of ICESat points used for validation is disjointed from the one used in the calibration process, in order to provide a correct data validation, as discussed in Section 2.6. Moreover, 11,340 geocells have been validated with less than 1000 overlapping validation points (for example, coastal regions, where geocells contain a significant water body and minimum land).

Fig. 15 shows an example of the absolute height error 90% confidence level evaluation for a single DEM geocell over California, USA. Subfigure (a) shows the location of the ICESat tracks: all available ICESat points are depicted in blue, while the used best 1000 are in red. It should be noted that almost no ICESat points are available over mountainous areas, since such points were already filtered out during the DEM calibration and mosaicking processing, due to unsatisfying quality. Subfigure (b) shows the histogram of the absolute value of the differences between TanDEM-X and ICESat in meters. The vertical green line identifies the 90% confidence level, which is located at 0.36 m.

Additionally to the ICESat data, DEM data have been validated using highly-accurate GPS tracks, as shown in (Wessel et al.,

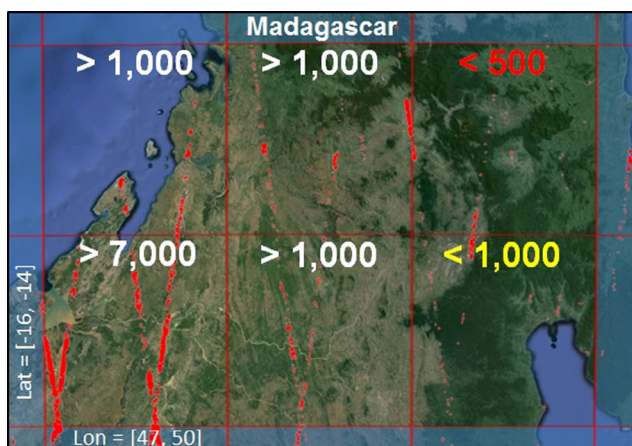


Fig. 14. ICESat tracks (bright red) superimposed on the border polygons of six TanDEM-X DEM geocells. Latitude/longitude frame coordinates: [16°S, 14°S], [47°E, 50°E].

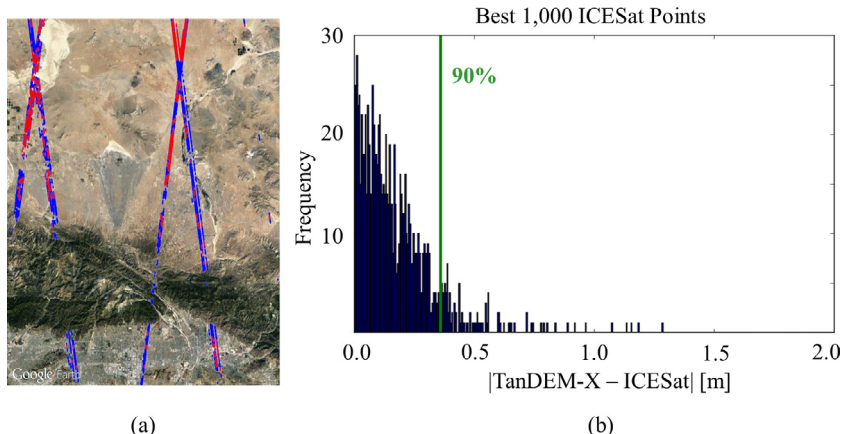


Fig. 15. (a) location of the ICESat tracks used for DEM validation for a geocell over California, USA: all available ICESat points are depicted in blue, while the used best 1,000 are in red. (b) histogram of the absolute value of the differences between TanDEM-X and ICESat. The vertical green line identifies the 90% confidence level, located at 0.36 m.

2014), which demonstrates a 90% linear accuracy of 1.93 m. Such value agrees with the obtained results from ICESat comparisons. In this paper we concentrate on the global validation using ICESat only, since the results in both cases are similar. Finally, even if not required by the mission specification, which relies on the globally accumulated height error statistics only, the absolute height accuracy is monitored on a geocell basis as well.

Global Results. The global geocell-based absolute height accuracy performance is presented in Fig. 16, while Fig. 17 shows the geocell-based mean height deviation. The validation could not be performed for the geocells identified in gray (not applicable). The reasons are either the lack of ICESat validation points, such as for latitudes lower than -88° in Antarctica or some mountainous regions in China, or land masses covering less than 1% of the considered geocell.

As mentioned at the beginning of this section, the accumulated Absolute Height Accuracy with 90% linear error can be separately evaluated for *Forest*, *Ice*, and *Generic* geocells. Looking at each subset separately, we start with the *generic* geocells which are not covered by ice or forest and which contain approximately 10 million validation points. The absolute height accuracy (90% linear error)

is an impressive 0.88 m and the mean height deviation is only 0.045 m. Next looking at the forest only case, the evaluation of the validation points shows a mean height deviation of 0.57 m and an absolute height accuracy again 90% linear error of 2.33 m. As this height difference is TanDEM-X height minus ICESat height, the positive mean height difference of 0.57 m over forested land means that the laser-based system of ICESat was able to penetrate the forest canopy until the ground, while the mean phase center of the radar-based TanDEM-X system is located close to the canopy. This effect can be seen in Fig. 17 in forested areas such as in Siberia. In the case of mainly ice covered geo cells the signal penetration offset between the laser-based ICESat data and the radar-based TanDEM-X height can be seen clearly in Fig. 17. In Greenland and Antarctica this difference in terms of penetration depth is so large that a dedicated calibration process had to be implemented, in which DEM calibration using ICESat was only performed on the rocky edges of the land mass and then extended to the center of the ice sheet (see Section 2.6).

As an example, Fig. 18 shows a comparison between the normalized histograms of TanDEM-X - ICESat differences for two different geocells: the one depicted in Fig. 15a (blue), located in

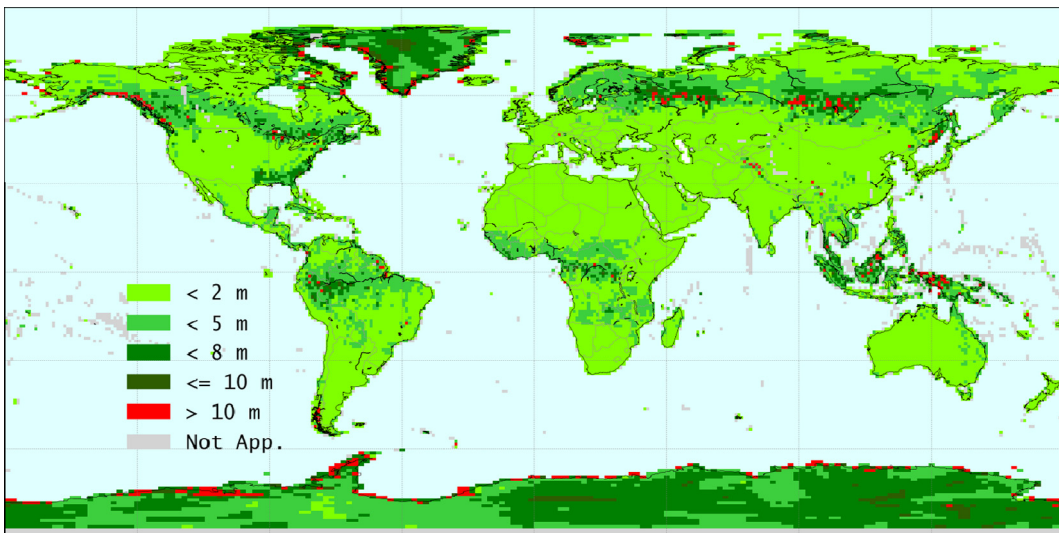


Fig. 16. Final TanDEM-X absolute height accuracy distribution at 90% confidence level. “Not Applicable” (gray) represents geocells where no validation points are available.

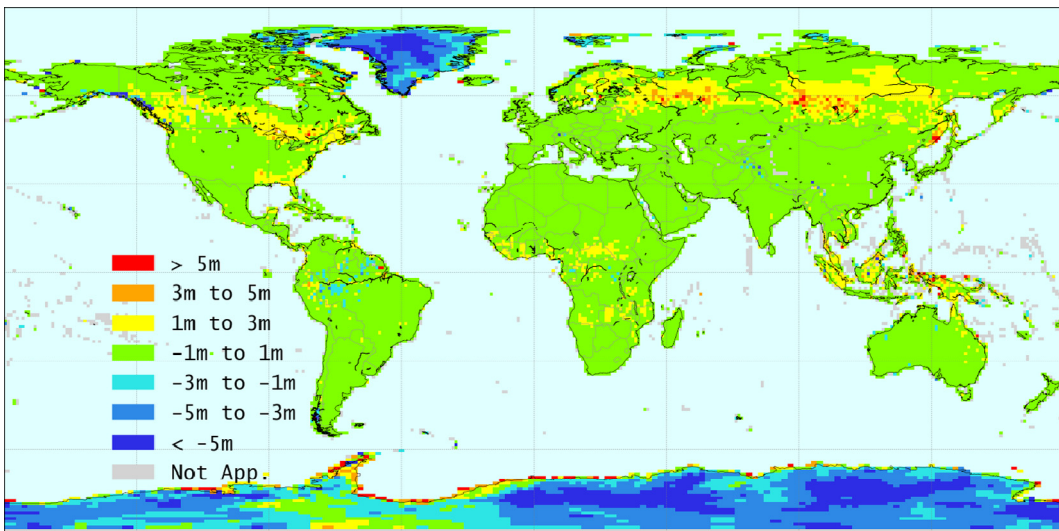


Fig. 17. Final TanDEM-X mean height accuracy distribution. “Not Applicable” (gray) represents geocells where no validation points are available.

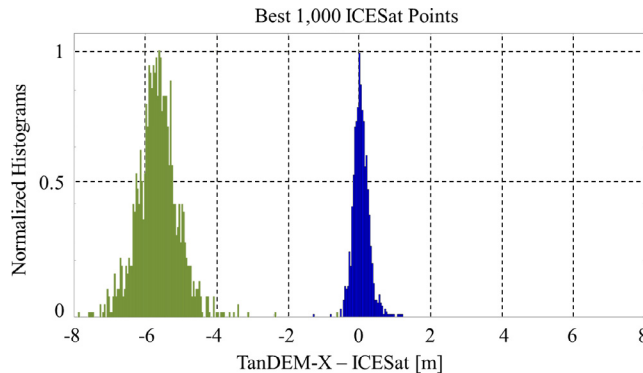


Fig. 18. Normalized histograms of the difference between TanDEM-X and ICESat for the DEM geocell in California depicted in Fig. 15 (a) (blue) and a DEM geocell located in the inner Greenland ice sheet (green).

California and characterized by the presence of bare soil, and a DEM geocell located in the inner Greenland ice sheet (green), dominated by the presence of dry snow. The histograms mean values are 0.07 m and −5.6 m, respectively, which clearly evidence the radar wave's penetration over snow-covered areas. Thus, as

expected, the absolute height accuracy in Greenland and Antarctica significantly increases to 6.37 m and the mean height error drops down to −2.83 m with some geocells going below −5 m.

Finally looking at the complete global performance, which also includes both ice and forest lands, the system specification of an absolute global height accuracy of 10 m (90% linear error) is well met and far exceeded with an overall accuracy of 3.49 m. The final absolute height statistics of the TanDEM-X DEMs for the different sub-sets are summarized in Table 2. The histograms for the different sub-sets of land in Fig. 19 are nearly symmetric for the case of generic land and show the described negative and positive shifts due to different penetration in ice and forest. Referring again to Fig. 16, out of 19,389 analyzed geocells, only 328 (or 1.69%) of them have an absolute height accuracy greater than 10 m. The vast majority of the geocells, over 10,954 or 56%, have an absolute height accuracy of less than 2 m.

3.2. Relative height accuracy

The relative height accuracy, or point-to-point vertical accuracy, describes the precision of the local height differences and accounts for random errors only. The relative vertical accuracy is a fundamental quality criterion for the selection of a DEM for many scient-

Table 2

Absolute height accuracy statistics, evaluated using the best 1000 ICESat validation points per DEM geocell. Such ICESat points tend towards moderate-relief terrain, as clarified in Section 3.1. Together with the overall performance (last column, bold), the evaluation is provided per generic, ice, and forest geocells, separately, defined as at the beginning of Section 3.

Statistics	Generic geocells	Ice geocells	Forest geocells	All geocells
Number of geocells	12,257	3,019	4,113	19,389
Landmass [km^2]	96.68 mil.	14.31 mil.	33.22 mil.	144.21 mil.
Accumulated number of validation points (millions)	10.20	2.71	2.58	15.49
Mean height deviation of validation points [m]	0.04	−2.83	0.57	−0.37
Accumulated absolute height accuracy of 10 m (linear error)	99.84%	98.42%	99.17%	99.48%
Accumulated absolute height accuracy with 90% linear error [m]	0.88	6.37	2.33	3.49

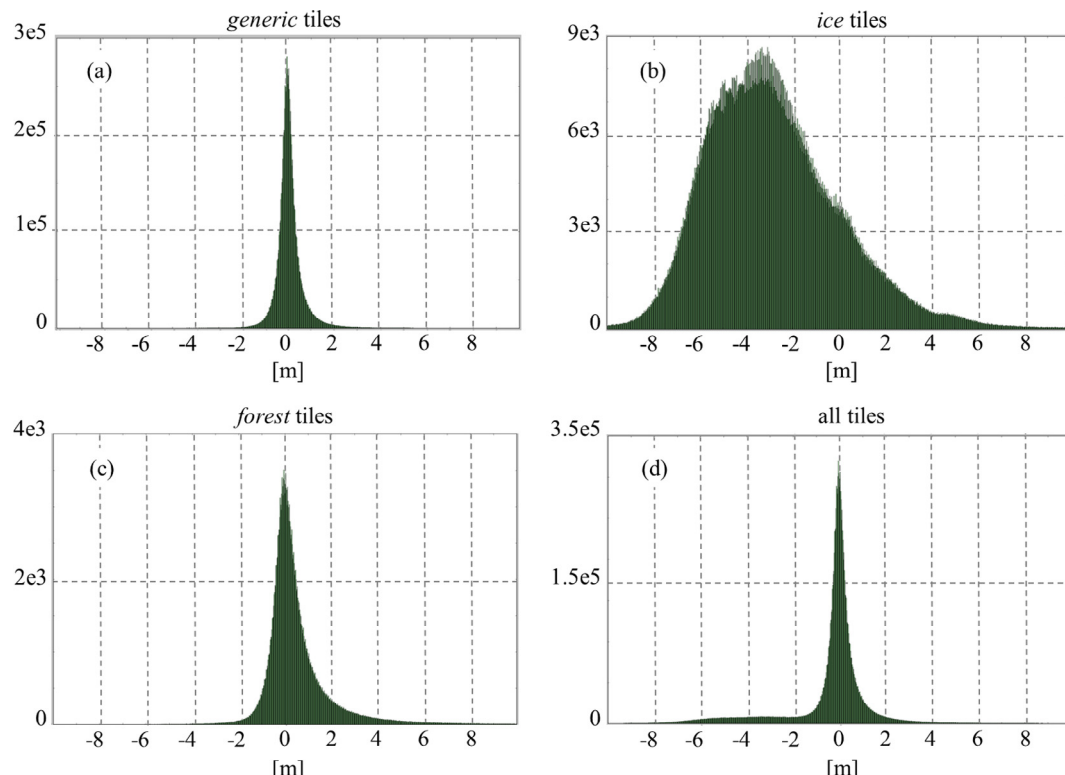


Fig. 19. Histograms of the absolute height accuracy for generic geocells (a), ice geocells (b), forest geocells (c), and all available geocells (d).

tific applications, especially the ones relying on the use of neighboring height differences, such as slope estimation, aspect calculation, and drainage networks (Jacobsen, 2010; Tarboton et al., 1991).

For a common area, such an error contribution can be directly estimated from the data by isolating the high frequency components of the difference between two DEMs, subsequently acquired with the same geometry and system parameters. This analysis was carried out over dedicated test sites during the TanDEM-X bistatic commissioning phase, and the obtained results are summarized in Rizzoli et al. (2012). Obviously, this approach cannot be implemented on a global scale, since repeatedly acquired DEMs are not available for the entire TanDEM-X coverage. The relative height accuracy had therefore to be estimated from the interferometric coherence, as presented in Bamler and Hartl (1998) and briefly summarized in the following. The results presented in Rizzoli et al. (2012) confirmed a good agreement between the two different methods. Nevertheless, it has to be kept in mind that the coherence-based approach does not account for additional phase unwrapping errors, which could further deteriorate the obtained performance.

The knowledge of the interferometric coherence γ and of the independent number of looks n , employed within the multilooking process, allows for the estimation of the interferometric phase error φ , whose probability density function (pdf) can be expressed as (Lee et al., 1994):

$$p_{\varphi}(\varphi) = \frac{\Gamma(n + \frac{1}{2})(1 - \gamma^2)^n \gamma \cos \varphi}{2\sqrt{\pi}\Gamma(n)(1 - \gamma^2 \cos^2 \varphi)^{n+\frac{1}{2}}} + \frac{(1 - \gamma^2)^n}{2\pi} F\left(n, 1; \frac{1}{2}; \gamma^2 \cos^2 \varphi\right), \quad (6)$$

where Γ is the gamma function and F is the Gauss hypergeometric function (Abramowitz and Stegun, 1965). The standard deviation of the interferometric phase errors can be expressed as:

$$\sigma_{\varphi} = \sqrt{\int_{-\pi}^{\pi} \varphi^2 p_{\varphi}(\varphi) d\varphi}. \quad (7)$$

For each mosaicked pixel within a TanDEM-X DEM geocell, the information on σ_{φ} is contained in the HEM layer and is evaluated as a weighted average of all input standard deviation estimates, derived from each single interferometric acquisition as in (7).

As mentioned in Krieger et al. (2007), the estimation of the point-to-point height error requires the computation of the difference between two random variables, where each one describes the fluctuation of the interferometric phase at one location, which corresponds to a convolution between the two pdfs $p_{\varphi}(\varphi)$. Assuming a zero mean Gaussian distribution, as justified in (Rizzoli et al., 2012), the point-to-point phase error standard deviation σ_{pp} between two independent height estimates is then derived as $\sigma_{pp} = \sqrt{2}\sigma_{\varphi}$.

The relative point-to-point vertical accuracy of a DEM, which is due to the fluctuation of the interferometric phase between two elevation estimates, can finally be expressed as (Krieger et al., 2007):

$$\Delta h = h_{amb} \frac{\sigma_{pp}}{2\pi}. \quad (8)$$

Evaluation Method. For TanDEM-X, the linear point-to-point relative height accuracy at a defined confidence level is determined from the mean cumulative density function derived from all available relative height error estimates as in Eq. (8). The overall confidence level of a DEM geocell is described as the percentage of all possible samples that can be expected to include the true population at the specified accuracy of 2 m for low-relief terrain (predominant

slope lower than 20%) and 4 m for high-relief terrain (predominant slope higher than 20%) (Gonzalez and Bräutigam, 2015), which, from now on, will be addressed as *flat* and *steep* terrain.

The estimation of the point-to-point confidence level for the specified height accuracy from the HEM layer of TanDEM-X delivered products can be performed using the method described in (Gonzalez and Bräutigam, 2015), which is briefly explained in the following:

1. First of all, the single-point relative height accuracy distribution of each i^{th} pixel is modeled as a Gaussian stochastic variable with zero mean and whose standard deviation σ_i is directly retrieved from the HEM layer.
2. In order to discriminate between *flat* and *steep* terrain, a threshold on the local slope is set. For this purpose, a map of mean local slope is generated at a resolution of 90 m × 90 m, by combining the horizontal and vertical gradients of the DEM, as detailed in Gonzalez and Bräutigam (2015).

For the j^{th} slope class (either *flat* or *steep* terrain), the sum of all available single-point relative height accuracy distributions, modeled as in step 1, is evaluated. For each slope class, the linear accuracy is then given by the mean cumulative probability density P_{\sum} . This can be computed by summing the probability density functions of all available pixels within the j^{th} slope class (where $i = [1, \dots, M_j]$ and M_j is the total number of pixels belonging to the j^{th} class):

$$P_{\sum}^j(\Delta h_j) = \sum_{i=1}^{M_j} \frac{1}{2\sqrt{\pi}\sigma_i} e^{-\frac{\Delta h_j^2}{4\sigma_i^2}} \quad (9)$$

where Δh_j is the height accuracy specification for the j^{th} slope class.

3. The third step consists of calculating the combined confidence level C as:

$$C = \frac{\sum_j \int_0^{\Delta h_j} P_{\sum}^j(\Delta h_j) d\Delta h_j}{\sum_j \int_0^{\infty} P_{\sum}^j(\Delta h_j) d\Delta h_j} \cdot 100\% \quad (10)$$

For the TanDEM-X case, Δh_j can be expressed as either $\Delta h_{flat} = 2$ m for *flat* terrain or $\Delta h_{steep} = 4$ m for *steep* terrain. It should be noted that only valid pixels are considered for the evaluation of the relative height accuracy (the meaning of valid/invalid pixels is explained in Section 3.3). The resulting confidence level of a geocell can now finally be compared to the 90% specification.

Finally, in order to gain a better understanding of the actual performance, it is also convenient to calculate the height accuracy for the 90% confidence level for *flat* and *steep* terrain separately as:

$$\frac{\int_0^{\Delta h_j} P_{\sum}^j(\Delta h_j) d\Delta h_j}{\int_0^{\infty} P_{\sum}^j(\Delta h_j) d\Delta h_j} = 0.9 \quad (11)$$

Global Results. An overview of the relative height accuracy of the final TanDEM-X DEM per geocell is shown in Fig. 20, as a confidence level map in percentage unit. All DEM geocells exceeding the 90% confidence level fulfill the specification. Geocells labeled in dark green and turquoise have an estimated confidence level under 90% and are either dominated by forest (more than 60%) or mostly covered by snow or ice. Such geocells are affected by volume decorrelation phenomena which artificially degrade the interferometric coherence. For this reason, they are disclaimed from the specification fulfillment. The same disclaimer is applied to geocells characterized by a large presence of water bodies (land below 0.1%), depicted in blue in Fig. 20.

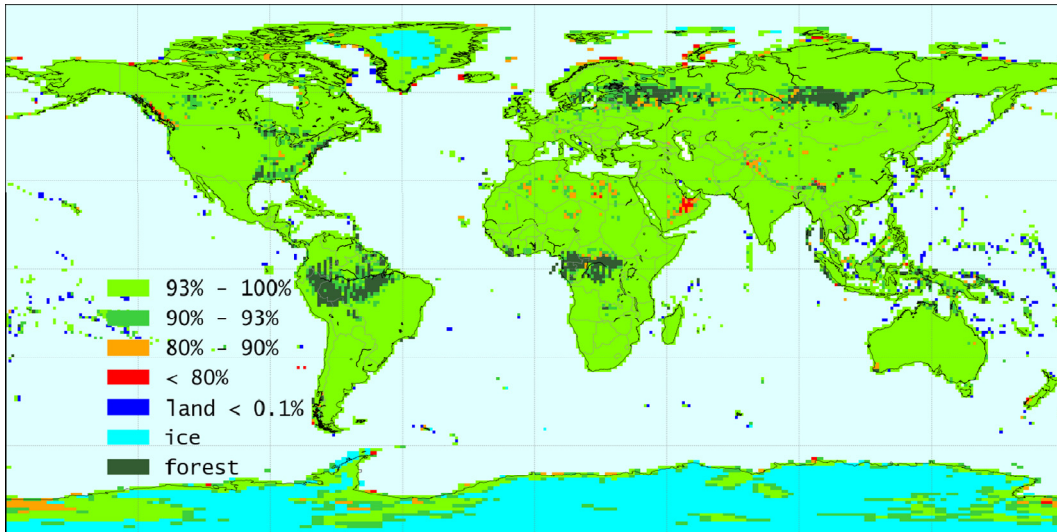


Fig. 20. Overall relative height accuracy in percentage confidence level for all TanDEM-X global DEM geocells, considering an accuracy specification of 2 m for low-relief terrain regions (local slopes up to 20%) and 4 m for high-relief terrain regions (local slopes higher than 20%).

The most critical regions are characterized by the presence of sandy deserts (e.g. the Sahara and the Arabian peninsula), due to a poor SNR. Nevertheless, the overall performance is very good even over most of these areas, thanks to the optimized re-acquisition strategy and processing, as explained in Section 2.5.

Of the 19,389 available TanDEM-X geocells, 16,205 have a relative height accuracy better than the required 90% confidence level. Of the remaining 3,184 products that are below 90%, 2,812 geocells are not considered to be reliable due to the disclaimers listed above. Hence, in the entire global TanDEM-X DEM dataset only 372 geocells, or 2.24% of the total geocells not associated with the disclaimers, do not meet the relative height accuracy specification. Detailed values are summarized in Table 3.

The histograms of the relative height accuracy at 90% confidence level for all 16,577 geocells not affected by the disclaimers is shown in Fig. 21. The blue and olive curves correspond to the histograms of flat and steep terrain areas within each geocell, respectively. The obtained quality is in most cases very good, achieving a relative height accuracy of about 1 m at the 90% confidence level for most of the geocells. The two vertical lines underline that more than 50% of all geocells have a relative height accuracy of less than 1 m over flat terrain regions, while about 70% of them have a relative height accuracy of less than 2 m over steep terrain regions.

As presented in Section 3.1, the relative height accuracy can be assessed with respect to the three land classes defined at the beginning of the section: forest, ice, and generic geocells (see

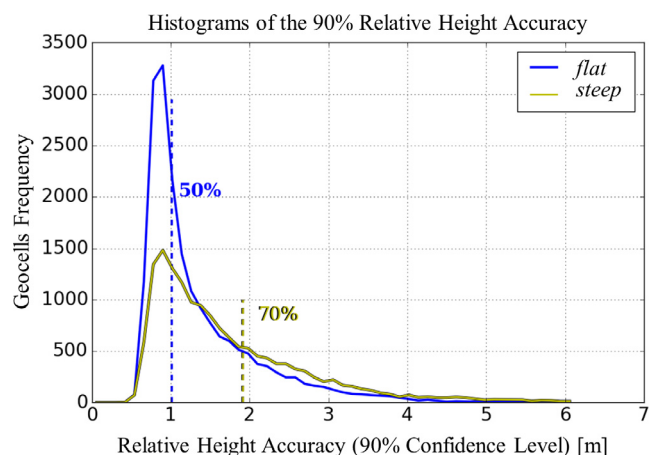


Fig. 21. Relative height accuracy distribution in meters for 19,389 TanDEM-X global DEM geocells, considering 90% confidence level for flat and steep terrain, respectively. No geocells are excluded.

Table 4

Relative Height Accuracy Statistics for TanDEM-X geocells, categorized by dominant ground classification type. The confidence level (second column) is evaluated by combining both flat and steep terrain as in Eq. (10). The last two columns show the relative height accuracy in meters at the 90% confidence level for flat and steep terrain separately, derived from Eq. (11).

Geocells	Confidence level [%]	Flat [m]	Steep [m]
Forest	94.38	1.63	1.93
Ice	82.24	2.72	2.41
Generic	98.27	0.99	1.37

Table 4. In this case, the confidence level within the specification has been evaluated by combining the entire set of available relative height accuracy estimations at a global scale and not on a geocell basis.

It has to be pointed out that geocells classified as ice belong almost entirely to either Greenland or Antarctica's ice sheets and are therefore predominantly characterized by the presence of

Table 3

Global Relative Height Accuracy Statistics. * These percentages are evaluated with respect to the total number of geocells not affected by the disclaimers (16,577).

DEM geocells	Count	Percentage [%]
Total	19,389	100
Total C < 90%	3,184	16.42
Total excluded by disclaimers	2812	14.50
Excluded by forest disclaimer	717	3.70
Excluded by ice disclaimer	1827	9.42
Excluded by land <0.1% disclaimer	268	1.38
Total without disclaimer	16,577	85.50
Without disclaimer and C < 90%	372	2.24*
Without disclaimer and C ≥ 90%	16,205	97.76*

snow- and ice-covered areas. Consequently, the evaluated confidence level in Table 4 provides a reliable representation of the performance characterizing this land cover type. The obtained results show an accuracy at the 90% confidence level which is slightly better over *steep* than over *flat* terrain (2.41 m vs. 2.72 m, respectively). The reason is the fact that *steep* terrain is mainly located at the outer borders of both Greenland and Antarctica ice sheets and characterized by the presence of either wet snow or bare ice and surface moraine. In these regions, the radar wave experiences a lower penetration into the snow pack than in the inner regions, characterized by the presence of dry snow (Rizzoli et al., 2017), while it does not penetrate at all over bare soil. This leads to higher values of the interferometric coherence and, therefore, to a better relative height accuracy.

On the other hand, for *forest* geocells, which are characterized by a relevant presence of vegetated areas (larger than 60%), the relative height accuracy is biased by the combination of all pixels within a single geocell, which might include a significant number of observations not classified as forest. For this reason, we further refined the classification approach for such geocells, in order to give a more reliable estimation of the global relative height accuracy over vegetated areas only.

For a single *forest* geocell, the ALOS PALSAR forest/non-forest map (Shimada et al., 2014) is applied to discriminate between forest (*F*) and non-forest (*NF*) pixels. The relative height accuracy is then evaluated for both kinds of pixels separately. An example is presented in Fig. 22, where, for the DEM geocell S04E018, situated between [3°S, 4°S] latitudes and [18°E, 19°E] longitudes, the TanDEM-X HEM is displayed (a), together with its corresponding forest/non-forest classification map (b). The obtained results are summarized in the first column of Table 5. A significant difference can be detected between the confidence level *C* for forest (*F*) pixels (89.30%) and non-forest (*NF*) ones (99.36%). Moreover, the relative height accuracy in meters at *C* = 90% is presented for both *flat* and *steep* terrain, separately. For this example, it should be mentioned that less than 0.1% of all land pixels are classified as *steep* terrain, leading to an unreliable statistic, due to too few input observations.

The same procedure has then been applied to about 3600 *forest* geocells and the global results, obtained by combining all available pixels from all geocells, are shown in the second column of Table 5. Overall, the considered forest areas show a relative height accuracy

Table 5

Relative Height Accuracy Statistics for TanDEM-X *forest* geocells, divided into vegetated (*F*) and non-vegetated (*NF*) ground classification types. The first column (Geocell S04E018) refers to the example presented in Fig. 22, while the second one reports the global performance.

Parameter	Geocell S04E018	Global perf.
<i>C F</i> [%]	89.30	92.60
<i>C NF</i> [%]	99.36	98.37
Acc. at <i>C</i> = 90% <i>F</i> , <i>flat</i> [m]	2.05	1.86
Acc. at <i>C</i> = 90% <i>F</i> , <i>steep</i> [m]	3.13	1.96
Acc. at <i>C</i> = 90% <i>NF</i> , <i>flat</i> [m]	0.86	0.96
Acc. at <i>C</i> = 90% <i>NF</i> , <i>steep</i> [m]	1.57	1.80

confidence level of 92.60%, while for non-forest ones it is well above 98%. In both cases, and for both *flat* and *steep* terrain, the overall height error accuracy at a 90% confidence level remains under 2 m.

3.3. Coverage statistics

Voids, i.e. invalid pixels, in DEM data arise when a pixel's height value cannot be determined during processing and can occur in a SAR system for various reasons, including missing acquisitions, low return signal power, or shadow/layover effects. The TanDEM-X final DEM is specified to the data coverage requirement shown in Table 1: the global data set can have up to 3% invalid data points (voids) over land (VOL).

Evaluation Method. The TanDEM-X DEM void pixels over land and water pixels are both flagged with the same invalid flag. In order to separate the voids over land from voids over water, a land/water body mask is needed. Between 56° south and 60° north latitudes the SRTM Water Body Data (SWBD), with a 30 m spatial resolution, is utilized for the majority of the geocells (SWBD, 2015). The SWBD does not contain information for a few geocells within desert regions and small islands, thus a second land mask is needed in these areas. For the remainder of the globe, including Antarctica, and for the missing areas in the SWBD, the European Space Agency's (ESA) Climate Change Initiative Land Cover (CCI - LC) data set is being utilized (CCIWB, 2015). The CCI-LC mask indicates the presence of open and permanent water bodies at a 300 m spatial resolution on a global scale.

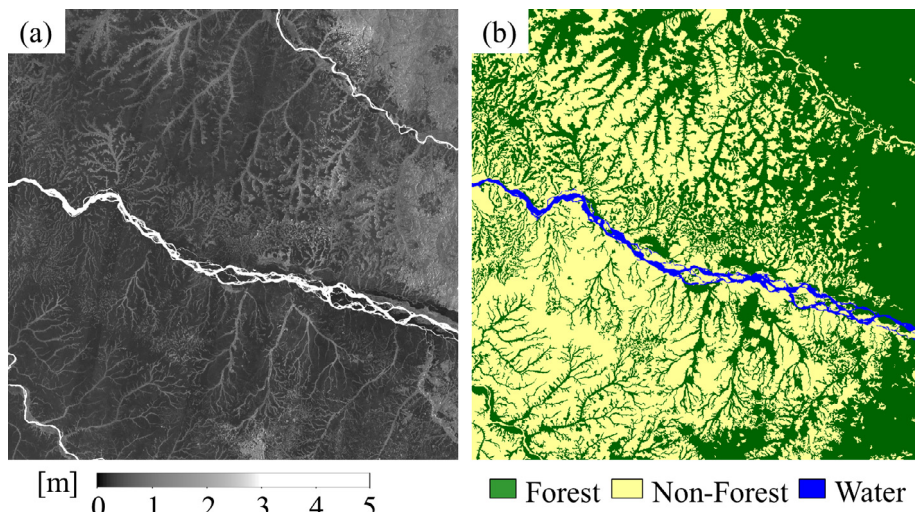


Fig. 22. (a) Height Error Map (HEM) for the TanDEM-X DEM geocell S04E018, located between [3°S, 4°S] latitudes and [18°E, 19°E] longitudes. (b) Corresponding ALOS PALSAR forest/non-forest classification map (Shimada et al., 2014).

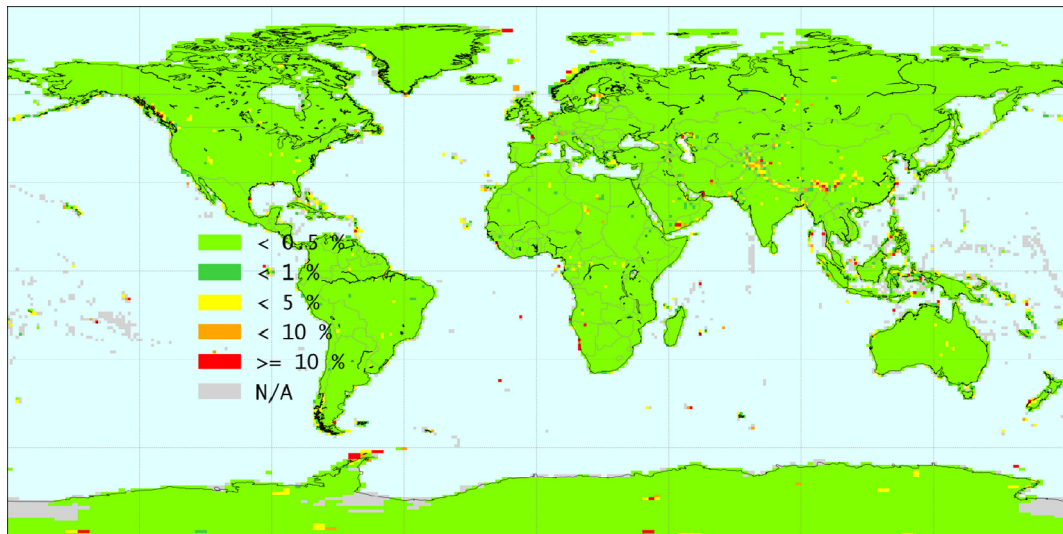


Fig. 23. Final TanDEM-X voids distribution. “Not Applicable” (gray) represents geocells where total land is less than 1% (e.g. dominated by the presence of water).

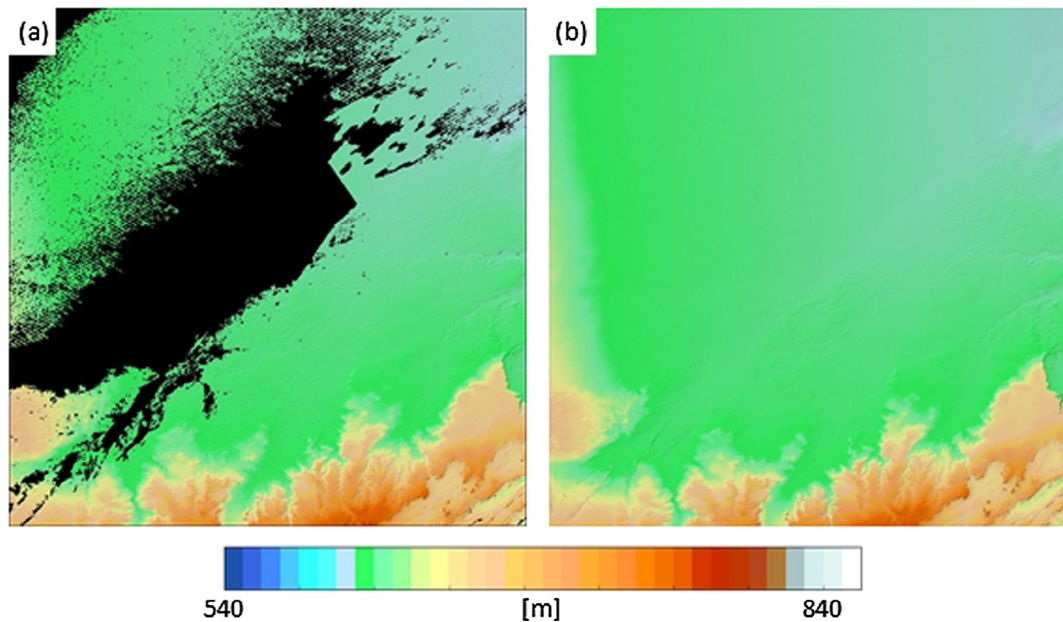


Fig. 24. SRTM unedited version 1.0 (a) and TanDEM-X (b) DEM at North 23.5° East 13.5° where black represents invalid data. In this case, the SRTM data contains over 25% voids whereas the CTanDEM-X data contains none (colorbar in meters).

Global Results. Of the total 19,389 geocells in the TanDEM-X dataset, voids over land account for only 0.107% of the entire data set. In other words, the data coverage is currently better than 99.89%. Fig. 23 shows the status of the global data coverage on a geocell level after removing geocells with land less than 1% (e.g. dominated by the presence of water). Over 67% of the geocells shown in this figure contain zero invalid data pixels. Furthermore, only 1366 or 7.0% of the geocells contain more than 1% of invalid pixels over land. Fig. 24 shows an example geocell of the data coverage for both the unedited SRTM Version 1.0 and the TanDEM-X in the Sahara desert centered at North 23.5° East 13.5°. Invalid data is depicted in black. In this example, the original SRTM data have a coverage of less than 75% whereas the TanDEM-X has full (100%) data coverage. This difference in void amount demonstrates the highly improved completeness of the TanDEM-X dataset, which is especially visible in the desert areas of the Sahara and the Middle

East, where TanDEM-X had performed at least two additional coverages with a steep viewing angle for an improved backscatter return (Martone et al., 2016a).

4. Conclusions

The TanDEM-X mission represents a milestone in spaceborne bistatic SAR missions. Thanks to the innovative close orbit formation of the TerraSAR-X and TanDEM-X satellite twins, bistatic spaceborne single-pass SAR interferometry has been performed for the first time.

The quality of the acquired data has been constantly monitored throughout the years, allowing for the development of an optimized acquisition and processing strategy, aimed at achieving the mission specification on the final global DEM accuracy. After

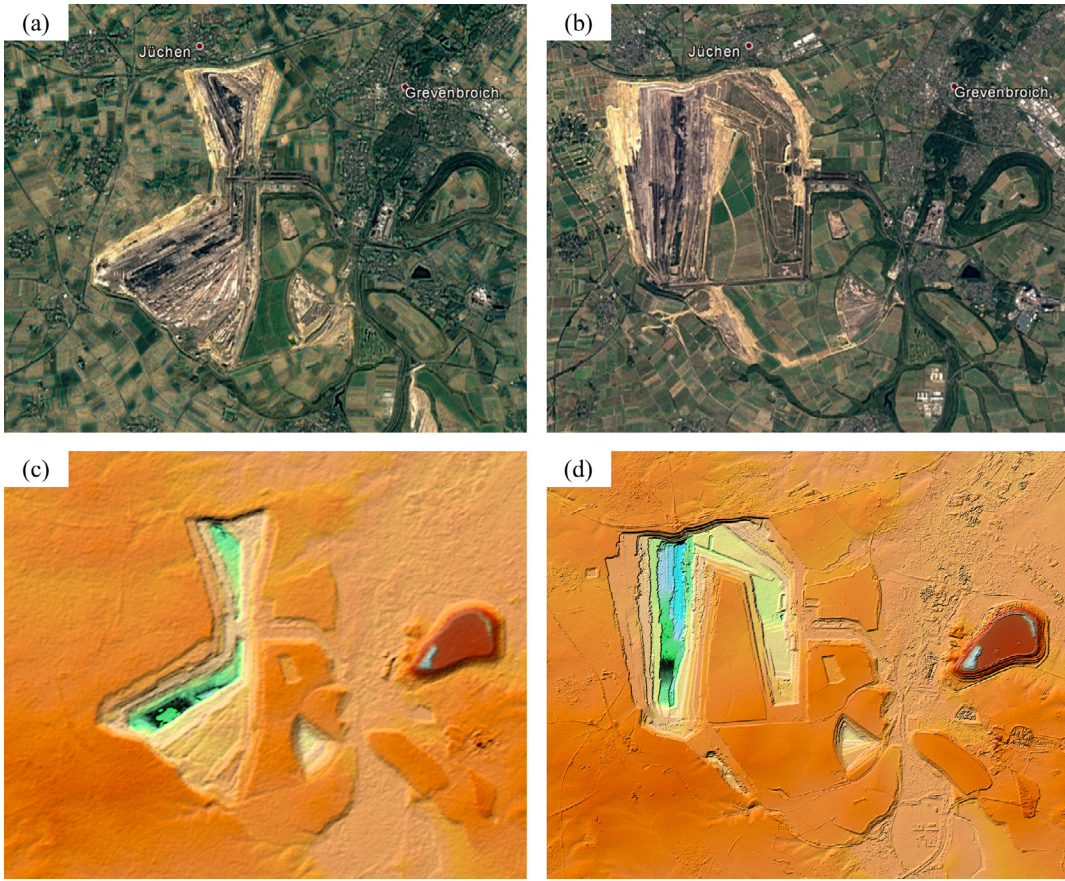


Fig. 25. Evolution of the Garzweiler mine in Germany. Optical images from © Google Earth from 2000 (a) and 2013 (b), respectively and corresponding SRTM (c) and TanDEM-X (d) DEMs.

six years of operation, the generation of the global DEM has been completed and its performance has been verified on a global scale.

The reported performance in terms of absolute vertical accuracy was performed using the best 1,000 ICESat validation points per DEM geocell, characterized by the lowest spatial variance and thus tending towards moderate-relief terrain. The obtained results confirm the outstanding capabilities of the system, with an overall absolute height accuracy at 90% confidence level of just 3.49 m, which is well below the 10 m mission specification. Excluding highly vegetated and snow-/ice-covered regions, characterized by radar wave penetration phenomena and consequently strongly affected by volume decorrelation, it improves to 0.88 m (for generic geocells only).

The users should be aware that this is a global statistic and local performance could be degraded, due to the presence of confined local outliers. An additional assessment procedure could be based on a comparison with locally available lidar DEMs, which offer better accuracy and improved coverage over mountainous terrain.

The relative height accuracy, which quantifies the random noise contribution within the final DEM, has been separately evaluated for both *flat* (predominant slope lower than 20%) and *steep* terrain (predominant slope higher than 20%). The mission specification at 90% confidence level (2 m and 4 m for *flat* and *steep* terrain, respectively) is met on a global scale for 97.76% of all geocells not disclaimed due to volume decorrelation effects. Moreover, more than 50% of all DEM geocells and about 70% of them show a relative height accuracy at 90% confidence level better than 1 m for *flat* terrain and better than 2 m for *steep* terrain, respectively. A dedicated analysis shows that, at a global scale, the relative height accuracy at 90% confidence level for vegetated areas remains under 2 m for both *flat* and *steep* terrain.

Finally, the performed analysis of the coverage statistics demonstrates that the final DEM is affected by the presence of only 0.1% of void pixels over land (VOL), which is significantly under the mission specification of 3% at a global scale.

The analysis of the global unedited TanDEM-X DEM product therefore confirms its stunning accuracy and global consistency and is now ready to be put forward as a new global topographic reference and be delivered to both the commercial and scientific communities.¹

Finally, the TanDEM-X data set represents a highly valuable starting point for monitoring the dynamic topographic changes of our planet. As an example, the evolution of the Garzweiler mine in Germany is briefly presented in Fig. 25, where SRTM and TanDEM-X DEMs from 2000 and 2013, respectively, are shown, allowing one to appreciate both the temporal update and the high level of details provided by the TanDEM-X system.

The TanDEM-X mission operation in bistatic mode has been recently extended until 2018, with the goal to generate an updated DEM and to monitor temporal changes.

Acknowledgment

The authors would like to acknowledge the extraordinary effort of all colleagues at DLR, Airbus Defence & Space, and the Helmholtz Centre Potsdam (GFZ) for making this ambitious idea a reality.

¹ Scientific proposals for accessing TanDEM-X mission data can be submitted at <https://tandemx-science.dlr.de/>.

References

- Abramowitz, M., Stegun, I., 1965. Handbook of Mathematical Functions. Dover, New York, NY, USA.
- Balss, U., Gisinger, C., Cong, X., Brcic, R., Hackel, S., Eineder, M., 2014. Precise measurements on the absolute localization accuracy of TerraSAR-X on the base of far-distributed test sites. In: EUSAR.
- Bamler, R., Hartl, P., 1998. Synthetic aperture radar interferometry. *Inv. Prob.* 14, R1–R54.
- Benson, C.S., 1962. Stratigraphic Studies in the Snow and Firn of the Greenland Ice Sheet. Research Report 70, U.S. Army Snow, Ice and Permafrost Research Establishment (Reprinted Aug. 1996).
- Borla Tridon, D., Bachmann, M., Schulze, D., Ortega-Miguez, C., Martone, M., Böer, J., Zink, M., 2013. TanDEM-X: DEM acquisition in the third year. *Int. J. Space Sci. Eng.* 1 (4), 367–381. M. D.P.
- Bräutigam, B., Hueso Gonzalez, J., Schwerdt, M., 2010. TerraSAR-X instrument calibration results and extension for TanDEM-X. *IEEE Trans. Geosci. Rem. Sens.* 48 (2), 702–715. Bachmann, February.
- Breit, H., Fritz, T., Balss, U., Eineder, M., Yague-Martinez, N., Rossi, C., 2010a. Processing of bistatic TanDEM-X data. In: IGARSS.
- Breit, H., Fritz, T., Balss, U., Lachaise, M., Niedermeier, A., Vonavka, M., 2010b. TerraSAR-X SAR processing and products. *IEEE Trans. Geosci. Rem. Sens.* 48 (2), 727–740.
- Breit, H., Lachaise, M., Balss, U., Rossi, C., Fritz, T., Niedermeier, A., 2012. Bistatic and interferometric processing of TanDEM-X data. In: EUSAR.
- Breit, H., Younis, M., Niedermeier, A., Grigorov, C., Hueso Gonzalez, J., Krieger, G., Eineder, M., Fritz, T., 2011. Bistatic synchronization and processing of TanDEM-X data. In: IGARSS.
- CCIWB, Nov. 2015. European Space Agency Climate Change Initiative global Water Bodies <<http://www.esa-landcover-cci.org/?q=node/162>>.
- Farr, T.G., Rosen, P.A., Caro, E., Crippen, R., Duren, R., Hensley, S., Kobrick, M., Paller, M., Rodriguez, E., Roth, L., Seal, D., Shaffer, S., Shimada, J., Umland, J., Werner, M., Oskin, M., Burbank, D., Alsdorf, D., 2007. The Shuttle Radar Topography Mission. *Rev. Geophys.* 45 (3/4), 1–33.
- Fritz, T., Eineder, M., Oct. 2013. TerraSAR-X Ground Segment Basic Product Specification Document. Technical Note 1.9, German Aerospace Center (DLR).
- Fritz, T., Rossi, C., Yague-Martinez, N., Rodriguez-Gonzalez, F., Lachaise, M., Breit, H., 2011. Interferometric processing of TanDEM-X data. In: IGARSS.
- GLOBCOVER, Jan. 2015. European Space Agency GlobCover Portal <<http://due.esrin.esa.int/globcover/>>.
- Gonzalez, C., Bräutigam, B., 2015. Relative height accuracy estimation method for InSAR-based DEMs. *IEEE J. Select. Top. Appl. Earth Observ. Rem. Sens.* 8 (11), 5352–5360. September.
- Gruber, A., Wessel, B., Huber, M., Roth, A., 2012. Operational TanDEM-X DEM calibration and first validation results. *IEEE J. Select. Top. Appl. Earth Observ. Rem. Sens.* 73, 39–49. Sep.
- Gruber, A., Wessel, B., Martone, M., Roth, A., 2016. The TanDEM-X DEM mosaicking: fusion of multiple acquisitions using InSAR quality parameters. *ISPRS J. Photogram. Rem. Sens.* 9 (3), 1047–1057. Mar.
- GTOPO, Oct. 2016. Global 30 arc-second Elevation (GTOPO30) <<https://lta.cr.usgs.gov/GTOPO30>>.
- Harding, D.J., Carabajal, C.C., 2005. ICESat waveform measurements of within-footprint topographic relief and vegetation vertical structure. *Geophys. Res. Lett.* 32 (21). November.
- Hastings, D.A., Dunbar, P.K., Elphingstone, G.M., Bootz, M., Murakami, H., Maruyama, H., Masaharu, H., Holland, P., Payne, J., Bryant, N.A., Logan, T.L., Muller, J.-P., Schreier, G., MacDonald, J.S., 1999. The Global Land One-Kilometer Base Elevation (GLOBE) Digital Elevation Model, version 1.0.
- Huber, M., Gruber, A., Wessel, B., Breunig, M., Wendleder, A., 2010. Validation of tie-point concepts by the DEM adjustment approach of tanDEM-X. In: IEEE International Geoscience and Remote Sensing Symposium, July, pp. 2644–2647.
- Huber, M., Wessel, B., Kosmann, D., Felbier, A., Schwieger, V., Habermeyer, M., Wendleder, A., Roth, A., 2009. Ensuring globally the TanDEM-X height accuracy: analysis of the reference data sets ICESat, SRTM and GPS-tracks. In: IEEE International Geoscience and Remote Sensing Symposium, pp. II-769–II-772.
- Hueso Gonzalez, J., Bachmann, M., Krieger, G., Fiedler, H., 2010a. Development of the TanDEM-X calibration concept: analysis of systematic errors. *IEEE Trans. Geosci. Rem. Sens.* 48 (2), 716–726. February.
- Hueso Gonzalez, J., Bachmann, M., Scheiber, R., Krieger, G., 2010b. Definition of ICESat selection criteria for their use as height references for TanDEM-X. *IEEE Trans. Geosci. Rem. Sens.* 48 (6), 2750–2757. July.
- Hueso Gonzalez, J., Walter, A., J.M., Bachmann, M., Krieger, G., Zink, M., Schrank, D., Schwerdt, M., 2012. Bistatic system and baseline calibration in TanDEM-X to ensure the global digital elevation model quality. *ISPRS J. Photogram. Rem. Sens.* 73, 3–11. June.
- ICESat, Oct. 2016. GLAS/ICESat laser altimetry digital elevation models (DEMs) of Antarctica and Greenland <https://nsidc.org/data/docs/daac/nsidc0304_0305_glas_dems.gd.html>.
- Jacobsen, K., 2010. DEM generation from satellite data. In: 3D Remote Sensing Workshop (EARSeL Ghent), pp. 21–29. September.
- Jezeck, K.C., 2002. RADARSAT-1 Antarctic mapping project: Change detection and surface velocity campaign. *Ann. Glaciol.* 34, 263–268.
- Krieger, G., De Zan, F., 2014. Relativistic effects in bistatic synthetic aperture radar. *IEEE Trans. Geosci. Remote Sens.* 52 (2), 1480–1488. Feb..
- Krieger, G., Moreira, A., Fiedler, H., Hajnsek, I., Werner, M., Younis, M., Zink, M., 2007. TanDEM-X: a satellite formation for high resolution SAR interferometry. *IEEE Trans. Geosci. Rem. Sens.* 45 (11), 3317–3341.
- Krieger, G., Zink, M., Bachmann, M., Bräutigam, B., Schulze, D., Martone, M., Rizzoli, P., Steinbrecher, U., Antony, J.W., De Zan, F., Hajnsek, I., Papathanassiou, K., Kugler, F., Rodriguez Cassola, M., Younis, M., Baumgartner, S., López-Dekker, P., Prats, P., Moreira, A., 2013. TanDEM-X: a radar interferometer with two formation-flying satellites. *Acta Astronaut.* 89, 83–98. August–September.
- Lachaise, M., Fritz, T., Balss, U., Bamler, R., Eineder, M., 2012. Phase unwrapping correction with dual-baseline data for the TanDEM-X mission. In: IEEE International Geoscience and Remote Sensing Symposium.
- Lachaise, M., Fritz, T., Breit, H., 2014a. InSAR processing and dual-baseline phase unwrapping for global TanDEM-X DEM generation. In: IEEE International Geoscience and Remote Sensing Symposium.
- Lachaise, M., Fritz, T., Eineder, M., 2014b. Dual-baseline phase unwrapping challenges in the TanDEM-X mission. In: EUSAR.
- Lee, J.S., Hoppel, K.W., Mango, S.A., Millerand, A.R., 1994. Intensity and phase statistics of multilook polarimetric and interferometric SAR imagery. *IEEE Trans. Geosci. Remote Sens.* 32 (5), 1017–1028. September.
- Martone, M., Bräutigam, B., 2015. Quantization effects in TanDEM-X data. *IEEE Trans. Geosci. Rem. Sens.* 53 (2), 583–597. K., G., June.
- Martone, M., Bräutigam, B., Rizzoli, P., Yague-Martinez, N., Krieger, G., 2016a. Enhancing interferometric SAR performance over sandy areas: experience from the TanDEM-X mission. *IEEE J. Sel. Topics Appl. Earth Observ. Remote Sens.* 9 (3), 1036–1046.
- Martone, M., Bräutigam, B., Rizzoli, P., Gonzalez, C., Bachmann, M., Krieger, G., 2012. Coherence evaluation of TanDEM-X interferometric data. *ISPRS J. Photogram. Remote Sens.* 73, 21–29. September.
- Martone, M., Rizzoli, P., 2016b. Volume decorrelation effects in TanDEM-X interferometric data. *IEEE Geosci. Rem. Sens. Lett.* G., K.
- Maurer, E., Kahle, R., Morfill, G., Schlepp, B., Zimmermann, S., 2014. Reversal of TanDEM-X's relative motion from counter-clockwise to clockwise. In: International Conference on Space Operation.
- Meyer, D., Tachikawa, T., Kaku, M., Iwasaki, A., Gesch, D., Oimoen, M., Zhang, Z., Danielson, J., Krieger, T., Curtis, B., Haase, J., Abrams, M., Crippen, R., Carabajal, C., Aug. 2011. ASTER global digital elevation model version 2 - summary of validation results. Technical report, NASA Land Processes Distributed Active Archive Center and Joint Japan-US ASTER Science Team.
- Moreira, A., Krieger, G., Hajnsek, I., Papathanassiou, K., Younis, M., Lopez-Dekker, P., Huber, S., Villano, M., Pardini, M., Eineder, M., De Zan, F., Parizzi, A., 2015. Tandem-L: a highly innovative bistatic SAR mission for global observation of dynamic processes on the earth's surface. *IEEE Geos. Rem. Sens. Magaz.* 3 (2), 8–23. Jul.
- Moreira, A., Krieger, G., Mittermayer, J., 2003. Satellitenkonfiguration zur interferometrischen und/oder tomographischen abbildung der erdoberfläche mittels radar mit synthetischer apertur (January).
- Moreira, A., Krieger, G., Mittermayer, J., January 2004. Satellite configuration for interferometric and/or tomographic remote sensing by means of synthetic aperture radar (SAR).
- Niemeier, W., 2002. Ausgleichsrechnung. Walter de Gruyter, Berlin.
- RAMP, 2016. Radarsat Antarctic Mapping Project Digital Elevation Model, version 2 (Oct) <<https://nsidc.org/data/nsidc-0082>>.
- Rizzoli, P., Bräutigam, B., Kraus, T., Martone, M., Krieger, G., 2012. Relative height error analysis of TanDEM-X elevation data. *ISPRS J. Photogram. Rem. Sens.* 73, 30–38. September.
- Rizzoli, P., Martone, M., Bräutigam, B., 2014. Global interferometric coherence maps from TanDEM-X quicklook data. *IEEE Geosci. Rem. Sens. Lett.* 11 (11). November.
- Rizzoli, P., Martone, M., Rott, H., Moreira, A., 2017. Characterization of snow facies on the greenland ice sheet observed by tanDEM-X interferometric SAR data. *Rem. Sens.* 9 (4).
- Rossi, C., Eieder, M., Fritz, T., 2014. Detecting building layovers in a SAR interferometric processor without external references. In: EUSAR.
- Rossi, C., Rodriguez Gonzalez, F., Fritz, T., Yague-Martinez, N., Eineder, M., 2012. TanDEM-X calibrated raw DEM generation. *ISPRS J. Photogram. Rem. Sens.* 73, 12–20.
- Rott, H., Sturm, K., Miller, H., 1993. Active and passive microwave signatures of antarctic firn by means of field measurements and satellite data. *Ann. Gacioil.* 17, 337–343.
- Schättler, B., Schwarz, E., Mrowka, F., Fritz, T., 2015. Serving the TerraSAR-X mission for over eight years: current status and recent extensions of the TerraSAR-X ground segment. In: 10th Advanced SAR Workshop.
- Schutz, B., Zwally, H., Shuman, C., Hancock, D., Di Marzio, J., 2005. Overview of the ICESat Mission. *Geophys. Res. Lett.* 32 (21).
- Shimada, M., Itoh, T., Motooka, T., Watanabe, M., Shiraishi, T., Thapa, R., Lucas, R., 2014. New global forest/non-forest maps from ALOS PALSAR data (2007–2010). *Rem. Sens. Environ.* 155, 13–31. May.
- SWBD, Dec. 2015. NASA Shuttle Radar Topography Mission Water Body Data <https://lpdaac.usgs.gov/dataset_discovery/measures/measures_products_table/srtmswbd_v003>.
- Tadono, T., Nagai, H., Ishida, H., Oda, F., Naito, S., Iwamoto, H., 2016. Initial validation of the 30 m-mesh global digital surface model generated by ALOS PRISM. *Int. Arch. Photogram. Rem. Sens. Spat. Inf. Sci.*, ISPRS XL-B4, 157–162. Minakawa.
- Tarboton, D.G., Bras, R.L., Rodriguez-Iturbe, I., 1991. On the extraction of channel networks from digital elevation data. *Hydrolog. Process.* 5 (1), 81–100. Nov..

- Touzi, R., Lopes, A., Bruniquel, J., Vachon, P.W., 1999. Coherence estimation for SAR imagery. *IEEE Trans. Geosci. Rem. Sens.* 37 (1), 135–149.
- Treuhhaft, R.N., Siqueira, P.R., 2000. The vertical structure of vegetated land surfaces from interferometric and polarimetric radar. *Radio Sci.* 35 (1), 131–177, January.
- Walter Antony, J., Hueso Gonzalez, J., Schwerdt, M., Bachmann, M., Krieger, G., Zink, M., 2013. Results of the TanDEM-X baseline calibration. *IEEE J. Select. Top. Appl. Earth Observ. Rem. Sens.* 6 (3), 1495–1501.
- Weber Hoen, E., Zebker, H., 2000. Penetration depths inferred from interferometric volume decorrelation observed over the greenland ice sheet. *IEEE Trans. Geosci. Rem. Sens.* 38 (6), 2571–2583, November.
- Wermuth, M., Montenbruck, O., Wendleder, A., 2011. Relative navigation for the TanDEM-X mission and evaluation with DEM calibration results. *22nd International Symposium on Spaceflight Dynamics*, vol. 78, pp. 103–108.
- Wessel, B., 2016. TanDEM-X Ground Segment DEM Products Specification Document. Technical Note 3.1, German Aerospace Center (DLR) (Aug.).
- Wessel, B., Bertram, A., Gruber, A., Bemm, S., Dech, S., 2016. A new highresolution elevation model of greenland derived from TanDEM-X. *ISPRS Ann. Photogramm. Remote Sens. Spatial Inf. Sci.* (July) 9–16.
- Wessel, B., Gruber, A., Huber, M., Breunig, M., Wagenbrenner, S., Wendleder, A., Roth, A., 2014. Validation of the absolute height accuracy of TanDEM-X DEM for moderate terrain. In: *IEEE International Geoscience and Remote Sensing Symposium*, pp. 3394–3397, July.
- Yague-Martinez, N., Eineder, M., Brück, R., Breit, H., Fritz, T., 2010. TanDEM-X mission: Sar image coregistration aspects. In: *EUSAR*.
- Zhu, S., Reigber, R., König, R., 2004. Integrated adjustment of CHAMP, GRACE, and GPS data. *J. Geod.* 78, 103–108.
- Zink, M., Buckreuss, S., 2015. TerraSAR-X and TanDEM-X mission status. In: *CEOS SAR CalVal*.
- Zwally, H.J., Schutz, R., Bentley, C., Bufton, J., Herring, T., Minster, J., Spinhirne, J., Thomas, R., 2009. GLAS/ICESat L2 Global Land Surface Altimetry Data, version 34 <<http://dx.doi.org/10.5067/ICESAT/GLAS/DATA227>>.